Title

Employing phosphonate and phosphinate ligands for prodrug development of the mitochondrial calcium uniporter inhibitor Ru265

Journal

Journal of Inorganic Biochemistry, 275

ISSN

0162-0134

Authors

Zou, Haipei

MacMillan, Samantha N

Wilson, Justin J

Publication Date

2026-02-01

DOI

10.1016/j.jinorgbio.2025.113145

Employing phosphonate and phosphinate ligands for prodrug development of the mitochondrial calcium uniporter inhibitor Ru265

Haipei Zou [a,b], Samantha N. MacMillan [a], Justin J. Wilson [a,b,*]

[a] *Department of Chemistry and Chemical Biology, Cornell University Ithaca, New York 14853, United States*

[b] *Department of Chemistry and Biochemistry, University of California Santa Barbara, Santa Barbara, California 93106, United States*

* *Corresponding author: justinjwilson@ucsb.edu*

Abstract

Ru265, $[Ru_2(\mu\text{-}N)(NH_3)_8Cl_2]Cl_3$, is a potent nanomolar inhibitor of the mitochondrial calcium uniporter (MCU), the transporter that mediates Ca^{2+} uptake into the mitochondria. This compound and related MCU inhibitors are promising therapeutic agents and chemical biology tools for studying intracellular Ca^{2+} dynamics. Axial ligand modification of these Ru-based complexes provides a facile way to tune their properties and make prodrugs. In this study, the use of axial phosphonate and phosphinate ligands was explored within this compound class, yielding $[Ru_2(\mu\text{-}N)(NH_3)_8(OPO(OH)Me)_2](CF_3SO_3)_3$ (**1**) and $[Ru_2(\mu\text{-}N)(NH_3)_8(OPOPh_2)_2](CF_3SO_3)_3$ (**2**). Both complexes were characterized by multinuclear NMR spectroscopy, revealing downfield shifts of the ^{31}P resonances of the coordinated ligands. The crystal structure of **1** was also obtained, which confirmed coordination of the methylphosphonate ligands to the axial sites of the Ru core. The aquation of **1** and **2** were studied by NMR and UV-vis spectroscopy. Unexpectedly, compound **1** undergoes partial aquation, arresting at a final product in which only one axial methylphosphonate is displaced by water. By contrast, **2** loses both diphenylphosphinates via aquation ($t_{1/2}$ = 1.7 h) under physiological conditions. The in vitro biological investigations of **1** and **2** in HeLa cells showed that neither demonstrate high cytotoxicity nor depolarize the mitochondrial membrane potential. Both compounds exhibit nanomolar inhibitory activity against mitochondrial Ca^{2+} uptake in permeabilized HEK293T cells and modest inhibitory activity against this process in intact HeLa cells. Notably, **1** shows pH-dependent activity for MCU inhibition, with greater inhibition in more acidic conditions, while **2** shows improvement in cellular uptake efficiency.

Keywords

metals in medicine, mitochondrial calcium uniporter, ruthenium, calcium, phosphorus-based ligands, nitrido ligands

1. Introduction

Calcium ions (Ca^{2+}) play a critical role in the regulation of many cellular functions through protein interactions and their capacity to act as signaling agents [1,2]. Consequently, maintenance of proper intracellular Ca^{2+} homeostasis is required for normal cell function. The mitochondria are important organelles that play a key role in this process [3,4]. Although the mitochondria have a high capacity for Ca^{2+}, excessive levels of this ion trigger a phenomenon known as mitochondrial Ca^{2+} ($_mCa^{2+}$) overload, which in turn leads to the opening of the mitochondrial permeability transition pore (MPTP), the generation of reactive oxygen species (ROS), and ultimately cell death [5,6]. Unsurprisingly, $_mCa^{2+}$ overload has been linked to a number of different pathological conditions such as neurodegenerative disorders [7–9], ischemia-reperfusion injury (IRI) [10–12], diabetes [13,14] and cancer [15,16].

Ca^{2+} entry into the mitochondria is mediated primarily by the mitochondrial calcium uniporter (MCU), an ion channel located in the inner mitochondrial membrane [17,18]. Given the deleterious effects of $_mCa^{2+}$ overload, the MCU has arisen as a promising drug target [19–21]. Consequently, there have been extensive efforts to identify MCU inhibitors that can be leveraged for therapeutic applications or as tools to study the role of the MCU in human diseases. Several recent high throughput studies of organic compound libraries have been successful in identifying new MCU inhibitors [22–29]. Although many of the newly found inhibitors cause secondary biological effects [24,30–34], the compound MCU-i11 has shown particular promise for its ability to inhibit $_mCa^{2+}$ uptake in intact cells and its apparent selectivity for MCU [20,24]. A notable feature of all of these organic inhibitors is their structural diversity, highlighting potential challenges for arriving at rational structure-activity relationships for new MCU inhibitors.

As an alternative approach, inorganic coordination complexes can also be used as MCU inhibitors. Most notably, the inorganic complex cation ruthenium red (RuRed, $[(NH_3)_5RuORu(NH_3)_4ORu(NH_3)_5]^{6+}$, Scheme 1) has long been studied for its ability to inhibit the MCU [35,36]. Most formulations of this compound, however, have poor purity [37,38], and researchers later found that the dinuclear Ru compound ruthenium 360 (Ru360, $[Ru_2(\mu\text{-}O)(HCO_2)_2(NH_3)_8]^{3+}$) was the key impurity that was responsible for the observed $_mCa^{2+}$ uptake inhibition [39–41].

Although Ru360 is a nanomolar inhibitor of the MCU, its use in complex biological systems is not straightforward. This compound is challenging to synthesize in its pure form [42], and is not stable in the presence of biological reducing agents, which in turn makes it impermeable to cells [43]. A new analogue of Ru360, called Ru265 ($[Ru_2(\mu\text{-}N)(NH_3)_8Cl_2]^{3+}$, Scheme 1), overcomes some of these limitations [44]. A key structural feature of Ru265 is its bridging nitrido (N^{3-}) ligand, which confers this complex with high stability to reducing agents [43]. This high stability has enabled its use as an MCU inhibitor for biological studies carried out in *in vitro* cell models [45–54], *ex vivo* brain slice models [45,55–58], and *in vivo* mouse models [45,52,59] in many labs. Because the chlorido ligands of Ru265 aquate within several minutes, the active species is believed to be Ru265′

($[Ru_2(\mu\text{-}N)(NH_3)_8(OH_2)_2]^{5+}$), a postulate that is support by molecular docking studies of this compound with the MCU [60]. Building upon the success of Ru265, subsequent analogues of this compound containing different axial ligands [61–64], as well as an osmium (Os) analogue [62,65], have been prepared (Scheme 1). The different axial-functionalized analogues of Ru265 not only undergo delayed aquation to active Ru265′, but also provide the opportunity to modify the lipophilicity of this compound and to introduce additional functionalities like fluorescence and redox activity.

To date, however, all of these analogues have relied on carboxylate-based axial ligands. Furthermore, they all rely on aquation for activation, a process that occurs on the timescale of hours. The use of alternative types of axial ligands could afford complexes with distinct activation pathways and timescales. In this study, we describe our studies on the use phosphonates ($RPO(OH)_2$) and phosphinates ($R_1R_2PO_2H$) as axial ligands for Ru265 prodrugs. Of particular interest is the availability of the –2 charge of the doubly-deprotonated phosphonate group. This dianionic charge may lead to stronger interactions with the dinuclear Ru core. Furthermore, the non-coordinating oxygen atom of the phosphonate could be susceptible to acid-base equilibria, allowing for the aquation process to be tuned by pH. The phosphinate group likewise provides a new type of axial ligand. An advantage of this scaffold is that it contains two different R groups, allowing for a greater degree of structural diversity of this compound class. This study presents the synthesis and characterization of two new Ru265 analogues with these ligands. A detailed study of their aquation is presented in conjunction with an investigation of their biological properties, highlighting the potential value of these ligand classes for new Ru-based MCU inhibitors.

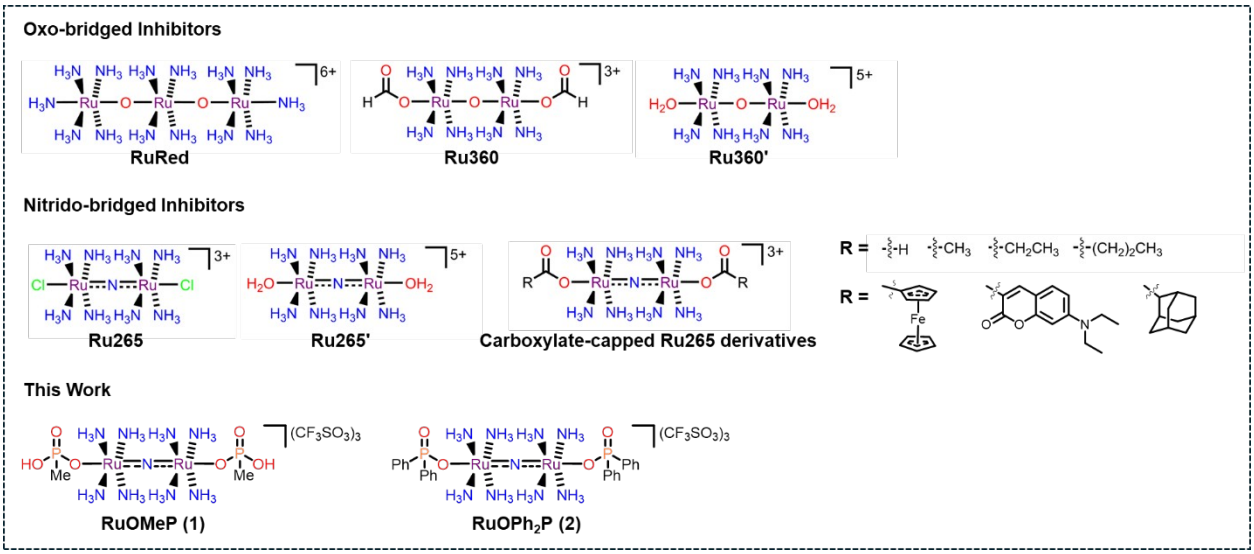

Scheme 1. The structures of Ru-based MCU inhibitors reported previously and the new Ru265 derivatives reported in this work.

2. Experimental section

2.1. Reagents and materials

All reagents and solvents were obtained commercially and used for synthesis without further purification. Ru265 and Ru265′ were prepared as previously described [44,63]. Water (18 MΩ·cm) was purified with an ELGA PURELAB flex 2 (High Wycombe, UK).

2.2. Physical measurements

NMR spectra were collected at 25 °C on a 500 MHz Bruker AV 3HD spectrometer equipped with a broadband Prodigy cryoprobe. NMR Chemical shifts (δ) are reported in units of parts per million (ppm). ^{1}H NMR chemical shifts were referenced internally to residual protic impurities within the DMSO-d_6 solvent, relative to tetramethylsilane at δ = 0 ppm. Chemical shifts in ^{31}P{^{1}H} spectra were referenced to external 85% H_3PO_4 at δ = 0 ppm, and ^{19}F chemical shifts are referenced to $CFCl_3$ at 0 ppm. UV-vis spectra were acquired on Shimadzu UV-1900 spectrometer (Shimadzu, Japan) equipped with a temperature-control unit using a circulating water bath. IR spectra were collected using Shimadzu IRSpirit-X spectrometer with QATR-S attachment (Shimadzu, Japan) and Bruker Tensor II IR spectrometer with a diamond ATR attachment (Bruker, MA). Lipophilicity of compounds were studied using analytical HPLC (Shimadzu, Japan). Elemental analysis (CHN) was performed by Atlantic Microlab (Norcross, GA) and the MSI Analytical Laboratory at UC Santa Barbara. Graphite furnace atomic absorption spectroscopy (GFAAS) was performed on a PinAAcle 900Z spectrometer (PerkinElmer, Waltham, MA) equipped with an AS900 furnace autosampler. Standard solutions (0–200 μg/L) of ruthenium(III) chloride were used to generate the calibration curve. The concentrations of all stock solutions of ruthenium compounds used for analytical or biological studies were determined by GFAAS. Absorbance and fluorescence of samples in a 96-well plate were measured using a BioTek Synergy HTX plate reader (Agilent, Santa Clara, CA). Fluorescence images of cells were taken using EVOS M5000 microscope (Thermofisher, USA) and Zeiss LSM 710 confocal microscope.

2.3. Synthesis of compounds

2.3.1. $[Ru_2(\mu\text{-}N)(NH_3)_8(OPO(OH)Me)_2](CF_3SO_3)_3\cdot 2H_2O$ (**1**·$2H_2O$)

To a stirring solution of Ru265′ (100 mg, 88.2 μmol) and methylphosphonic acid (16.9 mg, 176 μmol) in methanol (10 mL) was added triethylamine (18.4 μL, 132 μmol). The reaction mixture was stirred at 50 °C for 4 h. After cooling down to room temperature, the solvent was removed under vacuum, leaving a yellow residue. The yellow residue was suspended in 4 mL of tetrahydrofuran (THF), and the resulting yellow solid was collected by centrifugation. The solid was then dissolved in a minimal amount of methanol (~1 mL). THF was allowed to diffuse in the vapor phase into this solution at room temperature, affording an orange solid, which was washed sequentially with THF (3 × 3 mL) and diethyl ether (3 × 3 mL), followed by drying under vacuum. A quantity of 30 mg (29.3 μmol) of product as a yellow solid was obtained (yield: 33%). ^{1}H NMR (500 MHz, DMSO-d_6): δ 3.93 (s, 24H, NH_3), 1.13 (d, J(H,P) = 16.7 Hz, 6H, PCH_3). ^{13}C{^{1}H} NMR (126 MHz, DMSO-d_6) δ 120.68 (q, J(C,F) = 322.4 Hz, CF$_3$SO$_3^-$), 15.52 (d, J(C,P) = 138.5 Hz, PCH$_3$). ^{31}P{^{1}H} NMR (202 MHz, DMSO-d_6) δ 30.93. ^{19}F NMR (470 MHz, DMSO-d_6) δ –77.75. IR

(ATR, cm^{-1}): 3324 (m, br), 1648 (w), 1236 (s), 1216 (s), 1167 (s), 1027 (s). Anal. Calcd for $[C_2H_{32}N_9O_6P_2Ru_2](CF_3SO_3)_3 \cdot 2H_2O$: C, 5.86; H, 3.54; N, 12.29. Found: C, 6.04; H, 3.24; N, 12.13.

*2.3.2. Synthesis of $[Ru_2(\mu\text{-}N)(NH_3)_8(OPOPh_2)_2](CF_3SO_3)_3 \cdot 4Na(CF_3SO_3)$ (**2**·4Na(CF_3SO_3))*

A solution of Ru265′ (100 mg, 88.2 µmol) and sodium diphenylphosphinate (42.4 mg, 176 µmol) in methanol (10 mL) was stirred at 50 °C for 4 h. After cooling to room temperature, the solvent was removed under vacuum, resulting in an orange residue. This residue was dissolved in 4 mL of THF, and diethyl ether was allowed to vapor diffuse into it at 4 °C. Orange crystals were obtained after a week of vapor diffusion under these conditions. The solution was decanted, and the crystals were collected and subsequently washed with THF/diethyl ether (1:3, 2 × 3 mL) and diethyl ether (3 × 3 mL), followed by drying under vacuum. A quantity of 33 mg (17.2 µmol) of product as a yellow-to-orange solid was obtained (yield: 19%). ^{1}H NMR (500 MHz, DMSO-d_6): δ 7.68 (m, 8H), 7.41 (m, 12H), 3.89 (s, 24H). $^{13}C\{^1H\}$ NMR (126 MHz, DMSO-d_6) δ 138.61 (d, *J*(C,P) = 132.1 Hz, *ipso*-PPh*C*), 130.77 (d, *J*(C,P) = 9.5 Hz, *o*-PPh*C*), 130.63 (d, *J*(C,P) = 2.6 Hz, *p*-PPh*C*), 128.21 (d, *J*(C,P) = 12.0 Hz, *m*-PPh*C*), 120.68 (q, *J*(C,F) = 322.3 Hz, *C*$F_3SO_3^-$). $^{31}P\{^1H\}$ NMR (202 MHz, DMSO-d_6) δ 27.73. ^{19}F NMR (470 MHz, DMSO-d_6) δ –77.75. IR (ATR, cm^{-1}): 3322 (w, br), 1627 (w), 1226 (s), 1160 (s), 1115 (s), 1027 (s). Anal. Calcd for $[C_{24}H_{44}N_9O_4P_2Ru_2](CF_3SO_3)_3 \cdot 4Na(CF_3SO_3)$: C, 19.37; H, 2.31; N, 6.56. Found: C, 19.59; H, 2.68; N, 6.77. The number of $CF_3SO_3^-$ anion was confirmed by quantitative NMR spectroscopic analysis (Figure S12, Supplemental Data).

2.4. X-ray crystallography

Single crystals of **1** were obtained by the slow evaporation of a methanol solution of this compound at room temperature. Low-temperature X-ray diffraction data was collected on a Rigaku XtaLAB Synergy diffractometer coupled to a Rigaku Hypix detector with Cu Kα radiation (λ = 1.54184 Å) from PhotonJet micro-focus X-ray source at 102 K. The diffraction frames were processed and scaled on the CrysAlisPro software (Rigaku Oxford Diffraction, The Woodlands TX, 2015). The structure was solved through intrinsic phasing using SHELXT [66] and refined against F^2 on all data by full matrix least squares with SHELXL [67] following established refinement strategies [68]. All non-hydrogen atoms were refined anisotropically. Hydrogen atoms on the complex were positioned using a riding model. The isotropic displacement parameters of hydrogens in NH_3, OH and OH_2 groups were fixed at 1.2 times the equivalent isotropic displacement parameter of the nitrogen or oxygen atom, whereas those in CH_3 groups were set as 1.5 times relative to the carbon atom. An A-level CheckCIF alert highlighted the presence of a short (2.42 Å) intermolecular distance between phosphonate oxygen atoms on neighboring molecules in the crystal. Although a hydrogen atom could not be located in the difference Fourier map, its presence is inferred by this close interaction, which is presumed to be a symmetric hydrogen bond, and the necessity for charge balance in the crystal. The crystallographic data for **1** have been deposited with the Cambridge Crystallographic Data Centre (CCDC) under CCDC number 2493577 and can be accessed at http://www.ccdc.cam.ac.uk.

2.5. Measurement of compound lipophilicity

The logarithms of the partition coefficients (log *P*) of Ru-based compounds were determined using an HPLC-based method on a C-18 column [63,69]. An isocratic gradient of 25% MeCN in H_2O with 0.1% trifluoracetic acid was used as the elution solution. The dead time (t_0) of the column was determined by the retention time (t_r) of thiourea that has no interaction with C-18 column. A list of reference compounds with known log *P* values were eluted on the column and their retention factors log *k* ($k = (t_r - t_0)/t_0$) were correlated with their log *P* values by a linear standard curve. Ru-based compounds were eluted on the column using the same method, and their log *P* values were determined from their retention times from the standard curve.

2.6. UV-vis kinetic study

An aqueous solution of 20 μM of **2** in 4 mM of 3-(*N*-morpholino)propanesulfonic acid (MOPS) buffer (pH = 7.4) or 2-(*N*-morpholino)ethanesulfonic acid (MES) buffer (pH = 5.5) was incubated in a quartz cuvette at 37 °C. The UV-vis spectra of the solution were collected every 612 s for a time period of 17 h. The absorbance at 256 nm was monitored over time, and its decrease was fit to the first-order integrated rate law, from which the half-life of this process was calculated. The half-life was reported as average ± SD from three independent replicates.

2.7. NMR kinetic study

Aqueous solutions of **1** (600 μM) in 90 μM of MES buffer (pH = 5.5) or MOPS buffer (pH = 7.4) in a solution comprising 90% H_2O and 10% D_2O were incubated at 37 °C. The aquation kinetics of **1** were monitored by $^{31}P\{^1H\}$ NMR spectroscopy over time. The mol% of intact complex and free ligands were determined from the integral of $^{31}P\{^1H\}$ peaks.

2.8. Cell culturing

HeLa and HEK293T cell lines were obtained from American Type Culture Collection (ATCC, Washington DC) and cultured at 37 °C and 5% CO_2 with saturated humidity in a water-jacketed incubator. The cells were cultured in Dulbecco's Modified Eagle Medium (DMEM) supplemented with 10% fetal bovine serum (FBS) and passed every 2–3 days at 80–90% confluency. Cells were used for fewer than 30 passage cycles from their initial thawing. Mycoplasma tests were performed using Lonza's MycoAlert® Mycoplasma Detection Kit. All buffers and stock solutions used for cell work were sterile-filtered through a 0.2 μm polyethersulfone or cellulose membrane filter and maintained under sterile conditions.

2.9. Cytotoxicity assay

HeLa cells were seeded in 96-well plates with a density of ~2000 cells/well and incubated overnight for cells to attach. On the following day, cell culture media were replaced with 100 μL/well of cell culture media supplemented with test compounds of different concentrations and incubated for 72 h. Following incubation, the cell culture media were replaced with DMEM containing 1 mg/mL of 3-(4,5-dimethylthiazol-2-yl)-2,5-diphenyltetrazolium bromide (MTT) and incubated for 4 h. Media containing MTT was then removed, and the purple formazan crystals were dissolved in 200 μL of dimethyl sulfoxide and immediately subjected to absorbance measurement at 570 nm using a BioTek Synergy HTX plate reader. The average absorbance of untreated wells was

set as 100% cell viability, to which absorbance of treated wells was normalized and cell viability was determined. Dose-response curves between cell viability and drug concentration were generated and 50% growth inhibitory concentration (IC_{50}) values were determined based on six replicates from three independent trials.

2.10. Cellular uptake assay

HeLa cells were grown to confluency in a 6-well plate. On the day of experiment, media were replaced with 1 mL/well of cell culture media containing 0 or 50 μM of test compounds, and cells were incubated for 2 h. Following incubation, media were removed, and cells were washed with 1 mL of Dulbecco's phosphate-buffered saline (DPBS) followed by trypsin treatment. Cells were harvested, pelleted by centrifugation, and then washed with 1 mL of DPBS three times (via suspension in DPBS and centrifugation). Following the washing cycle, cell pellets were suspended in 300 μL of 3-((3-cholamidopropyl) dimethylammonio)-1-propanesulfonate (CHAPS) lysis buffer (1% w/v CHAPS, 5 mM EDTA, 50 mM TRIS and 100 mM NaCl, pH = 7.4). The suspension was vortexed for 10 s and rocked on ice for 30 min. Following incubation, cells debris were removed by centrifugation. The ruthenium concentration of the supernatant was measured by GFAAS, and the protein content was measured by bicinchoninic acid (BCA) assay (Pierce™ BCA Protein Assay Kits, ThermoFisher). Cellular uptake of test compounds was reported as average mass ratio of ruthenium normalized to protein (pg Ru/μg protein) from three independent replicates.

2.11. Mitochondrial membrane potential via JC-1 Assay

This procedure was adapted from previous literature [70,71]. HeLa cells were seeded on an 8-well μ-slide (ibidi, USA) at a density of 1×10^4 cells/well and incubated overnight at 37 °C. On the next day, cell culture medium was replaced with cell culture medium supplemented with 0 or 50 μM of test compounds, and the cells were incubated for 24 h. Following this incubation, cell culture medium was replaced with medium containing 10 μM JC-1 dye and incubated in the dark for 30 min at 37 °C. Dye-containing medium was then removed, and cells were washed with 2 × 200 μL DPBS. A quantity of 200 μL DPBS supplemented with 50 μM carbonyl cyanide *m*-chlorophenyl hydrazone (CCCP) was added to wells acting as a positive control, and 200 μL DPBS was added to negative and compound-treated wells. Cells were then immediately imaged using an EVOS M5000 microscope (Thermofisher, USA). Green fluorescence from JC-1 monomers was imaged using a GFP LED light/filter cube (470/22 nm Ex; 510/42 nm Em), whereas red fluorescence from JC-1 aggregates was imaged using a Texas Red LED light/filter cube (585/29 nm Ex; 624/40 nm Em). The fluorescence images of cells were analyzed in ImageJ [72]. The red/green ratio of corrected total cellular fluorescence (CTCF) of cells were determined from 10 cells and reported as average ± SD, where CTCF is defined via the following equation

$$CTCF = Integrated\ Density - (Area\ of\ Selected\ Cell \times Background\ Mean\ Fluorescence)$$

where integrated density is the total pixel intensity within cells, area of selected cell is the 2D space occupied by a cell, and background mean fluorescence is the pixel intensity normalized per unit area of regions of the image that do not contain cells.

2.12. $_{m}Ca^{2+}$ uptake assay in permeabilized cells

HEK293T cells were grown to near confluency in a T75 cell culture flask. On the day of the experiment, cells were harvested using trypsin/EDTA and isolated via centrifugation. The cell pellet was suspended in ice-cold DPBS containing 5 mM EDTA, and the cells were counted using trypan blue and an automated cell counter (Countess™, ThermoFisher). Cells were pelleted by centrifuging at 600 × *g* for 5 min at 4 °C and then suspended in permeabilization solution consisting of high KCl buffer (125 mM KCl, 20 mM 4-(2-hydroxyethyl)-1-piperazineethanesulfonic acid (HEPES), 2 mM K_2HPO_4, 5 mM glutamate, 5 mM malate and 1 mM $MgCl_2$, pH = 7.4) supplemented with 80 μM digitonin and 1 μM thapsigargin. This cell suspension was rocked on ice for 25–30 min to allow for the digitonin to permeabilize their outer membranes. Cells were pelleted by centrifuging at 220 × *g* for 10 min at 4 °C. Cells were then suspended in imaging solution consisting of high KCl buffer supplemented with 2 mM sodium succinate and 1 μM Calcium Green-5N to make a cell suspension with a cell density of 1×10^7 cells/mL. The experiment was performed on a black 96-well plate. Each well contained 100 μL of cell suspension (~1×10^6 cells/well) supplemented with different concentrations of test compounds. Fluorescence emission from Calcium Green-5N (ex. 488 / em. 528) was measured at 37 °C using a BioTek Synergy HTX plate reader. Background fluorescence was monitored for 3 min before 5 μL of $CaCl_2$ solution (20 μM bolus) was added to each well. The change of fluorescence in response to Ca^{2+} was measured every 8 s for a course of 3 min. The cycle of $CaCl_2$ addition and fluorescence monitoring was repeated three times in each well. The rate constant of Ca^{2+} uptake in each well was determined by fitting the fluorescence decay trace with a first order exponential decay equation. The untreated well with the highest Ca^{2+} uptake rate represented 0% inhibition. Inhibition of treated wells was determined by normalizing the Ca^{2+} uptake rate constant to that of untreated wells. Dose-response curves between inhibition and drug concentration were generated, and IC_{50} values were determined from three independent replicates.

2.13. Time and pH-dependent $_{m}Ca^{2+}$ uptake assay in permeabilized cells

Aqueous solutions of 20 μM of **1** and **2** in 4 mM of MES buffer (pH = 5.5) or MOPS buffer (pH = 7.4) were incubated at 37 °C. The incubation of **1** was quenched by flash freezing in $N_2(l)$ after time points of 0, 2, 4, 6, 24 h, while the incubation of **2** was quenched by flash freezing in $N_2(l)$ after time points of 0, 0.5, 2, 6, 12 h. The samples were stored at –20 °C until needed for the experiment. The $_{m}Ca^{2+}$ uptake assay in permeabilized cells was performed as described before, where cells were treated with the thawed flash frozen solutions of **1** at a final concentration of 20 nM or **2** at a final concentration of 15 nM. The $_{m}Ca^{2+}$ uptake rate was determined via a more sensitive method by calculating the slope of linear fitting of the first 5 data points of each trace, in order to better distinguish the inhibitory difference from different treatment groups. Values are reported from three independent replicates.

2.14. $_{m}Ca^{2+}$ uptake assay in intact live cells

The procedure was adapted from previous studies [73–76]. A quantity of 1×10^5 HeLa cells was seeded on a 35-mm glass bottom dish with poly-D-lysine coating (MatTek, USA) and incubated

overnight at 37 °C. On the day of the experiment, cell culture medium was removed, and cells were incubated in cell culture medium supplemented with 0, 10, or 50 μM of test compounds for 2 h. After drug incubation, cells were washed with 1 mL of DPBS and then incubated in 1 mL of extracellular medium (ECM, 135 mM NaCl, 20 mM HEPES, 5 mM KCl, 1 mM $MgCl_2$ and 1 mM $CaCl_2$, pH = 7.4) supplemented with 1 μM Rhod2-AM, 0.003% Pluronic F127, 10 mM glucose and 2 mg/mL bovine serum albumin (BSA) at room temperature in dark for 30 min. Dye-containing solution was removed, and cells were washed with 1 mL of ECM, followed by incubation in fresh ECM containing 10 mM glucose and 2 mg/mL BSA at room temperature for 30 min. Cells were then washed with 1 mL of ECM again and incubated in fresh ECM containing 10 mM glucose and 2 mg/mL BSA at 37 °C for 10–15 min before imaging with a Zeiss LSM 710 confocal microscope. The sample was excited at 561 nm and emission was collected at 565–712 nm. Fluorescence images (50 frames) of cells were taken every 3 s to monitor the concentration change of $_{m}Ca^{2+}$. After a baseline monitor for ~30 s, 1 mL of ECM solution containing 200 μM histamine and 10 mM glucose was carefully added to the dish, and the change of fluorescence was monitored. The fluorescence images of cells were analyzed in ImageJ [72]. The CTCF values were determined from 6 cells and reported as average ± SD. Experiments were repeated to confirm reproducibility.

2.15. Computational studies

DFT calculations were performed on Gaussian 16 [77]. The geometry optimization of monoaquated **1** cation, $[Ru_2(\mu\text{-}N)(NH_3)_8(OPO(OH)Me)(OH_2)]^{4+}$, was carried using the hybrid B3LYP functional [78,79]. The 6-31G(d,p) basis set was used for light elements (H, C, N, O, P) [80,81], whereas the LANL2DZ effective core potential and its associated basis set were employed for Ru [82]. The initial structure of monoaquated **1** cation was modified from the crystal structure of **1** for geometry optimization. The optimization was carried in the gas phase without symmetry constraints. Frequency calculations were performed to confirm the structure was optimized to local minimum of the potential energy surface, as indicated by the absence of imaginary frequencies. Cartesian coordinates of the optimized structures are provided in Supplemental Data (Table S3). The docking study between the DFT-optimized structure of the monoaquated **1** cation and the MCU binding pocket was performed on HERMES using the GOLD program [83]. The binding site of the MCU (PDB 6O5B) [84] was defined as the centroid of the four aspartate and the four glutamate residues at the opening pore of MCU. Residues within 10 Å of the defined binding site were included for docking analysis. Monoaquated **1** cation was subjected to 100 cycles of genetic algorithm runs using ChemPLP [85] as the scoring function to evaluate the results. All other parameters were set as default.

3. Results and discussion

3.1. Synthesis and characterization

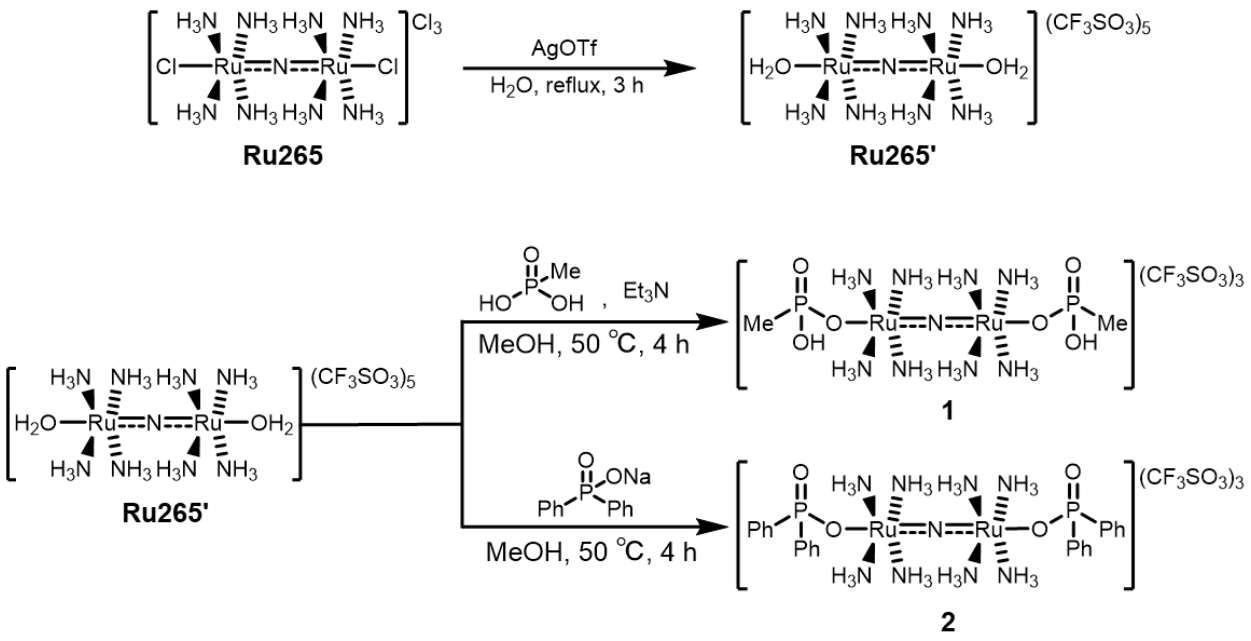

Scheme 2. Reaction schemes for the synthesis of Ru265' and Ru265 derivatives **1** and **2**.

As a proof-of-concept study to investigate the use of axial phosphonates and phosphinates for Ru265 prodrugs, the commercially accessible acids methylphosphonic acid and diphenylphosphinic acid were used in this work. The new Ru265 derivatives were synthesized using a similar strategy that has been employed to access carboxylate-capped analogues [61–64]. In this process, Ru265 was treated with 5 equivalents of silver triflate to remove the inner- and outer-sphere Cl^- anions as insoluble AgCl, affording the diaqua-capped Ru265′ (Scheme 2). The more labile aqua ligands of Ru265′ could be substituted by treating this compound with 2 equivalents of methylphosphonic acid or sodium diphenylphosphinate to obtain **1** and **2** (Scheme 2), which were characterized by multinuclear NMR spectroscopy in DMSO-d_6 (Figures S2–S12, Supplemental Data). The ^{1}H NMR spectra of **1** and **2** reveal the protons of the equatorial NH_3 ligands to resonate at 3.93 and 3.89 ppm, respectively. These chemical shifts are upfield to those of the chlorido-capped Ru265 (4.15 ppm) [44]. This shift is comparable to those found within previously reported Ru265 derivatives with axial aqua or carboxylate ligands [61–64]. Changes within the ^{31}P NMR chemical shifts also occur upon coordination. Within **1**, the ^{31}P resonance of the phosphonate ligand shifts from 25.87 to 30.93 ppm upon complexation. For **2**, a similar change is observed as the ^{31}P resonance of the phosphinate ligands moves from 24.11 to 27.73 ppm. These downfield shifts are similar to those observed within other mononuclear phosphonate and phosphinate complexes of Ru [86,87]. Both compounds show a single ^{19}F peak at –77.75 ppm, which is attributed to the outer-sphere triflate counterions. Although mass spectrometry measurements were attempted, peaks corresponding to the parent ions could not be readily identified. The failure to observe these peaks is most likely a consequence of the high charges of these ions, which would require ionization with different counteranions, as well as fragmentation of the parent ions.

The crystal structure of **1** confirms the expected structure for this complex cation, revealing direct coordination of the phosphonate ligands in the axial positions (Figure 1, Tables S1–S2, Supplemental Data). In addition, the bridging nitrido ligand resides on a crystallographic inversion center, conferring the complex with C_i symmetry and a perfectly linear Ru–N–Ru backbone. The crystallographic inversion center also enforces an eclipsed arrangement of the equatorial NH_3 ligands. In other crystal structures of Ru265 analogues, both eclipsed and staggered arrangements of these ligands have been observed, indicating that there is most likely a small energy difference between them and that subtle factors in the crystal lattice, like hydrogen bonding, can influence the observed structure [88]. The interatomic distance between each Ru center and the bridging nitrido is 1.73451(17) Å, a value that is not appreciably different from related Ru265 derivatives [61–64]. The interatomic distance between the Ru center and the O of the axial phosphonate is 2.095(2) Å. In a previously reported dinuclear metal-metal bonded Ru complex containing axial phosphonate ligands, the average interatomic distance between the axial phosphonate ligands and Ru centers is 2.23 Å [89], which is significantly longer than these distances in **1**. This difference is attributed to the stronger trans influence of the metal-metal bond and lower charge density on the mixed-valent Ru(II)–Ru(III) bridge compared to the Ru(IV)–N–Ru(IV) bridge. The Ru–O interatomic distance in **1** falls within the range of those reported for carboxylate-capped Ru265 derivatives (2.076–2.119 Å) [61–64], consistent with the similar ionic radii of the oxygen donor atoms found in both ligand classes. The Ru-phosphonate interaction is also supported by a hydrogen bond between the P=O of the phosphonate ligand and an equatorial NH_3 ligand. In addition, there is a close intermolecular interaction between the neighboring molecules of **1** between the phosphonate oxygen atoms O3. This distance is only 2.42 Å (Figure S1, Supplemental Data), markedly shorter than conventional hydrogen-bonding interactions [90]. This close interaction is mediated by a proton on the inversion center, which could not be located in the difference Fourier map, that gives rise to symmetric hydrogen bonding. A similar intermolecular symmetric hydrogen bond was observed in the crystal structure of Ru360' [42] and the mixed-valent Ru(II)–Ru(III) phosphonate complex [89] as well.

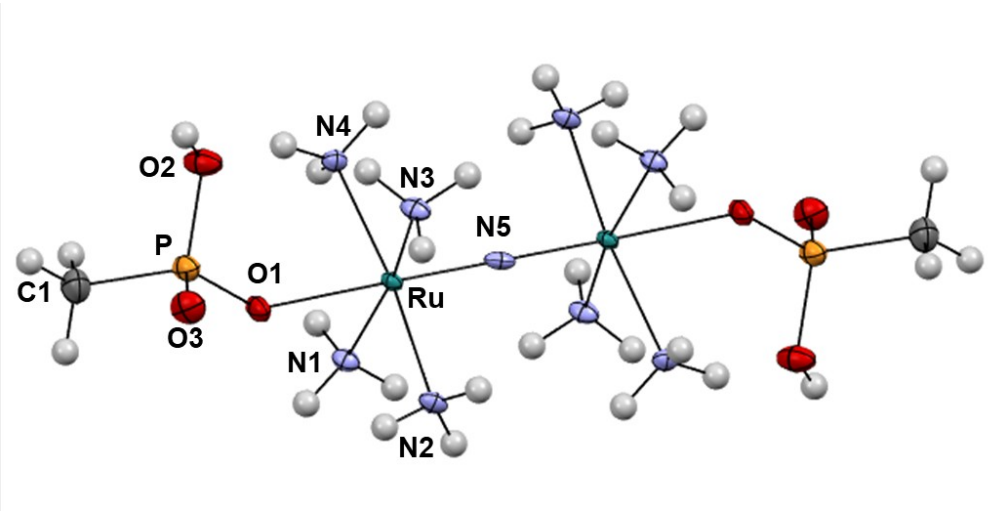

Figure 1. The crystal structure of **1**. Thermal ellipsoids are shown at the 50% probability level. Solvent and counterion molecules are omitted for clarity. In addition, a hydrogen atom, posited to be shared by the O3 atoms of adjacent molecules, is also not shown.

3.2. Physical properties

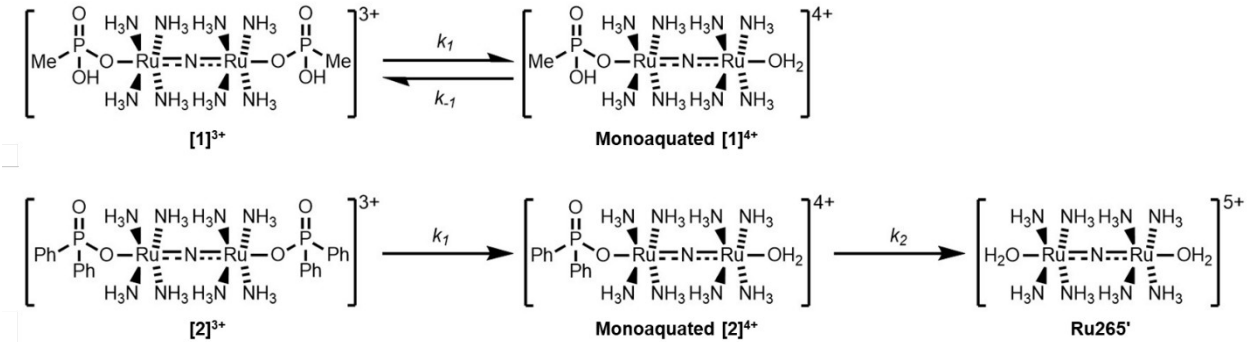

Scheme 3. Aquation pathways of the Ru265 analogues **1** and **2**.

The Ru265 derivatives **1** and **2** are designed to be prodrugs that can undergo aquation to release Ru265′ (Scheme 3). To assess their suitability for this application, we measured the kinetics of this process. The aquation of **1** under physiological conditions (pH = 7.4 and 37 °C) was monitored by $^{31}P\{^{1}H\}$ NMR spectroscopy (Figure 2a). These spectra reveal a time-dependent intensity increase of the resonance corresponding to the free phosphonic acid at 23.1 ppm concomitant with the intensity decrease of the resonance corresponding to the intact complex at 29.5 ppm. In addition, a third peak at 29.3 ppm forms at the same rate and extent as the free ligand signal. This third peak is therefore assigned to the phosphonate ligand of the monoaquated form of **1**. As shown in Figure 2b, **1** and its aquation products reach equilibrium after ~30 h. At equilibrium, 60% of **1** undergoes aquation, only forming the monoaquated product. This result is in contrast to prior studies of carboxylate-capped Ru265 analogues, where the aquation process to form Ru265′ reached completion [61–64].

The observation that only one phosphonate ligand of **1** is displaced by water indicates that the Ru-phosphonate bond is more thermodynamically stable than the Ru-carboxylate bond within these Ru265 analogues. A key difference between methylphosphonic acid as an axial ligand in **1** compared to the previous carboxylate analogues is that methylphosphonic acid is a diprotic acid. The two acidic OH groups of the ligand have pK_a values of 2.12 and 7.29 [91]. As shown in the crystal structure, the methylphosphonate binds to the Ru centers in a monodentate fashion, leaving the second OH group susceptible to deprotonation. Upon coordination to Ru, the acidity of this second OH group should increase, leading to a pK_a value of <7.29. Therefore, at physiological pH = 7.4, the non-coordinated OH group should primarily be deprotonated, thus making the ligand dianionic. The higher charge of the ligand will strengthen its electrostatic interactions with the Ru centers, leading to a more thermodynamically stable bond. To investigate this hypothesis, the aquation of **1** was probed under acidic conditions (pH = 5.5 and 37 °C). At pH = 5.5, the $^{31}P\{^{1}H\}$ resonances of all species are shifted downfield from their values measured at pH = 7.4 (Figure 2a). This downfield shift is most likely a consequence of the protonation equilibria of the methylphosphonic acid, based on the precedence that oxyphosphorus acids are known to exhibit pH-dependent ^{31}P NMR chemical shifts [92].

As shown in Figure 2a, the aquation process of **1** proceeds more quickly and to a larger extent at pH 5.5 compared to pH 7.4 at equilibrium, which is reached in approximately 17 h with 67% of **1** converted to the monoaquated species. Even at these lower pH conditions, however, the formation of Ru265′ was not detected, indicating that the aquation stops after loss of the first ligand. A more quantitative analysis of this aquation process at both pH 7.4 and 5.5 was carried out by fitting the $^{31}P\{^{1}H\}$ NMR data to the integrated rate laws for a reversible A ⇌ B + C reaction (Equation 1 and Equations S1–S9, Supplemental Data). As summarized in Table 1, the rate constant k_1 and equilibrium constant K_{eq} for **1** at pH 5.5 are both larger than those measured under physiological pH 7.4, suggesting that increased protonation of the methylphosphonic acid ligand favors its dissociation. Therefore, the methylphosphonate ligands of **1** provide a distinct activation pathway compared to the carboxylate-capped Ru265 analogues that we have previously studied. Overall, **1** undergoes aquation more slowly than the carboxylate-capped analogues, and is unique in that it forms a stable monoaquated complex. The protonation equilibria of this ligand also lead to pH-dependent aquation, a feature that can potentially be exploited for targeting acidic tissues or organelles.

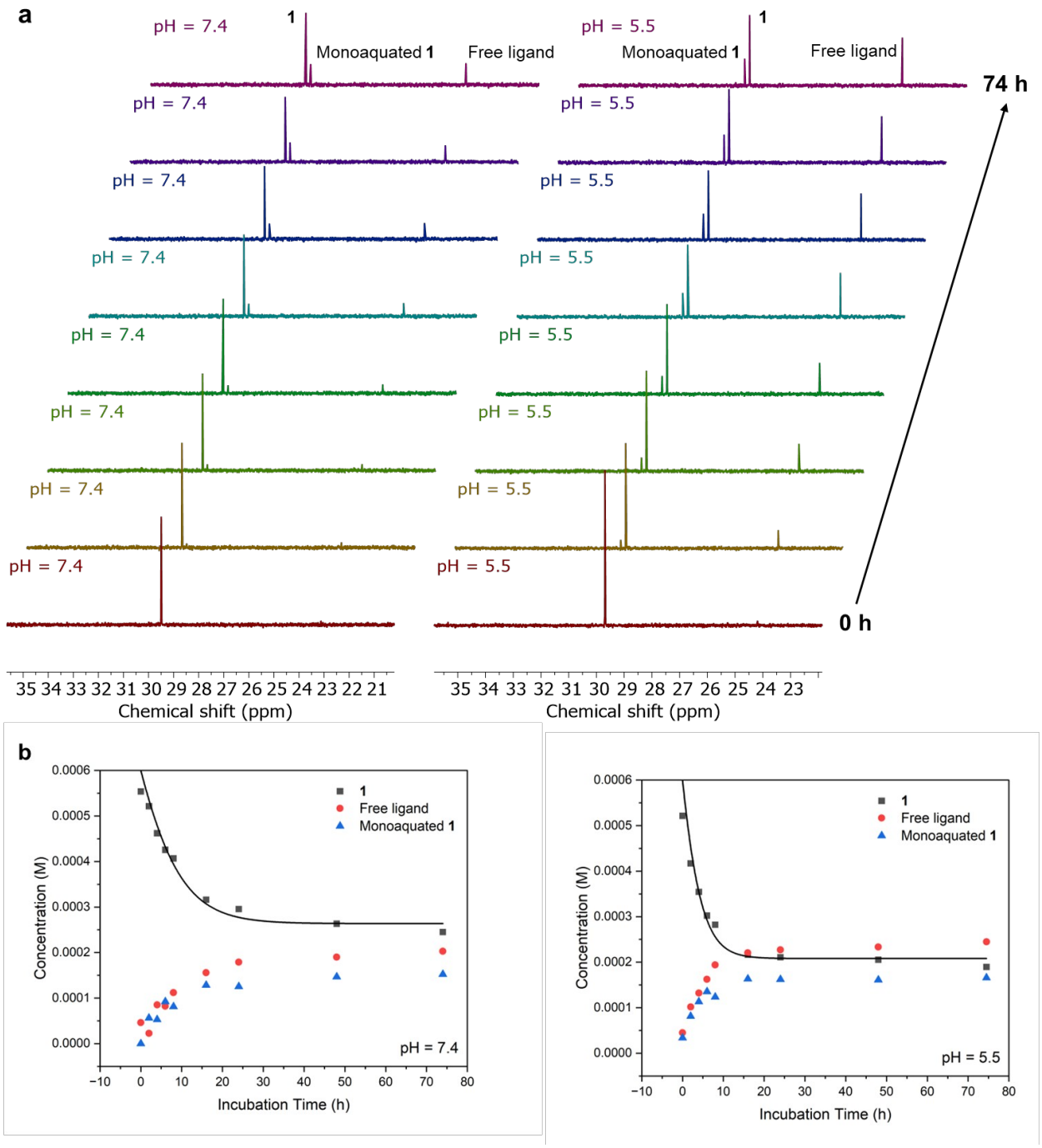

Figure 2. The aquation kinetic analysis of **1** via $^{31}P\{^{1}H\}$ NMR spectroscopy at 37 °C in MOPS buffer (pH = 7.4) or MES buffer (pH = 5.5) containing 10% D_2O. (a) $^{31}P\{^{1}H\}$ resonance of each species formed during aquation are shown. (b) The change of concentration of each species is plotted over time.

$$A \underset{k_{-1}}{\overset{k_1}{\rightleftharpoons}} B+C$$

$$[A]_t=[A]_0-\frac{-k_1+\sqrt{\Delta}}{2k_{-1}}\times\frac{1-\exp\left(-t\sqrt{\Delta}\right)}{1+\frac{\sqrt{\Delta}-k_1}{\sqrt{\Delta}+k_1}\exp\left(-t\sqrt{\Delta}\right)} \quad (1)$$

$$where\,[A]_0=600\,\mu M\,,\Delta=\sqrt{k_1^2+4k_1k_{-1}[A]_0}$$

Table 1. Aquation rate constants (k_1 and k_{-1}), equilibrium constants (K_{eq}) and half-lives ($t_{1/2}$) of **1** at 37 ° under different pH.

	$k_1 \times 10^{-2}$ (h^{-1})	k_{-1} ($M^{-1}h^{-1}$)	$t_{1/2}$ (h)	$K_{eq} \times 10^{-4}$ (M)
pH = 7.4	6.8 ± 1.3	155.1 ± 38.6	5.3 ± 1.0	4.4 ± 0.4
pH = 5.5	15.4 ± 1.8	193.3 ± 10.0	2.8 ± 0.3	7.9 ± 0.6

Next, the aquation of **2** was investigated. The time-dependent $^{31}P\{^1H\}$ NMR spectra of this compound in MOPS buffer (pH = 7.4) at 37 °C was acquired (Figure 3a). The ^{31}P resonance of **2** at 33.6 ppm decayed over time, and a new peak at 23.4 ppm, corresponding to free diphenylphosphinate, grew over the course of 22.5 h. In addition, a small signal at 32.7 ppm could be identified at early timepoints. This species is assigned to be the monoaquated species, an intermediate on path to the fully aquated Ru265′. A similar monoaquate intermediate could be detected during the aquation of the carboxylate-capped Ru265 analogues [61]. In these prior studies, the rate constant for the first ligand dissociation step was significantly smaller than that for the second, resulting in almost no accumulation of the monoaquated intermediate during the reaction. Based on the similarly low amounts of the monoaquated intermediate of **2** detected, the same situation is true for this compound.

Because the rate-determining step for aquation is the first ligand loss, UV-vis spectroscopy can be used as a simple way to approximate the half-life and first aquation rate constant for these complexes. A UV-vis analysis of **2** in MOPS buffer (pH = 7.4) and MES buffer (pH = 5.5) at 37 °C revealed a time-dependent decrease in the absorbance band at 256 nm (Figure 3b and 3c). The changes in absorbance at this wavelength could be fit to monoexponential function, consistent with a pseudo first order process. The half-lives of **2** in physiological ($t_{1/2}$ = 1.7 ± 0.2 h) and acidic ($t_{1/2}$ = 1.9 ± 0.1 h) conditions are equivalent within error, indicating that **2** does not have pH-dependent aquation kinetics within this pH range. These half-life values are smaller than those of the previously reported carboxylate-capped analogues, whose aquation half-lives range between 3.3–9.9 h. Therefore, compound **2** is more labile than the carboxylate-capped analogues and the phosphonate-capped compound **1**. The different kinetics of these complexes appears to be related to the pK_a values of the axial ligands. The pK_a of diphenylphosphinic acid is 2.3, which is lower than

those of the conjugate acids of the axial carboxylate ligands that we previously studied, reflecting the lower basicity of this ligand that presumably leads to more labile coordination bonds with Ru.

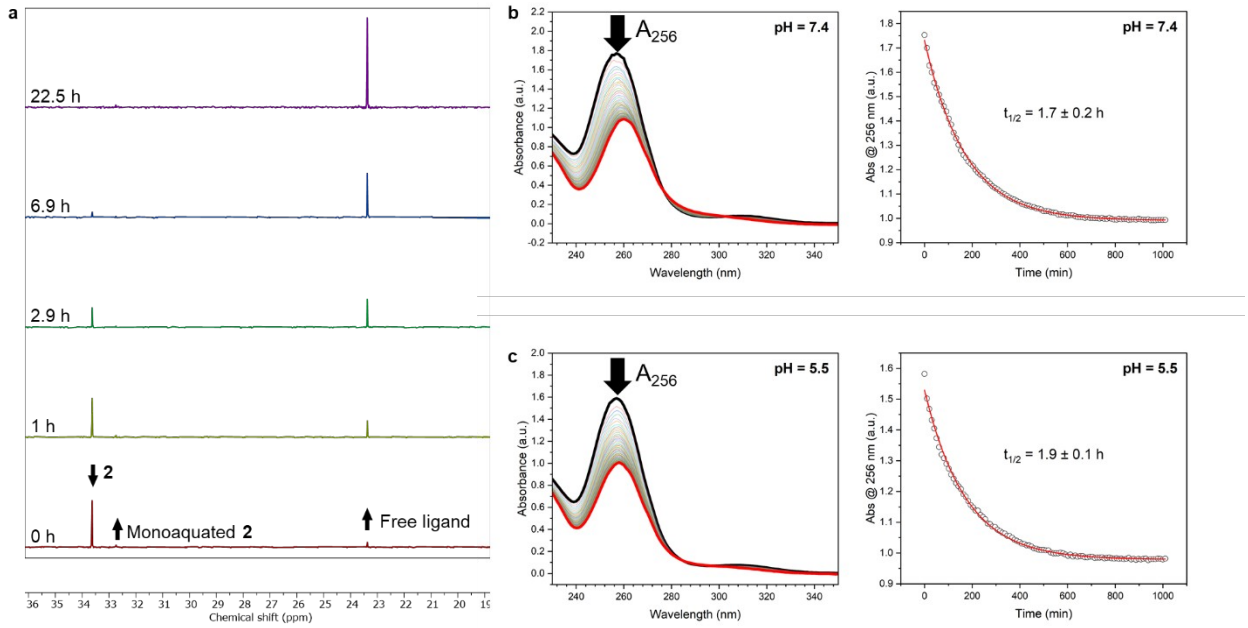

Figure 3. The aquation kinetics of **2** monitored by $^{31}P\{^{1}H\}$ NMR (containing 10% D_2O) and UV-vis spectroscopy. (a) $^{31}P\{^{1}H\}$ resonance of each species formed during aquation in MOPS buffer (pH = 7.4) at 37 °C are shown. (b) UV-vis spectra of **2** collected every 10.2 min during aquation in MOPS buffer (pH = 7.4) at 37 °C. (c) UV-vis spectra of **2** collected every 10.2 min during aquation in MES buffer (pH = 5.5) at 37 °C. The absorbance changes at 256 nm are tracked over time.

The lipophilicity of a compound can have significant effects on its cell permeability and localization properties. We have previously shown that axial ligand modifications to Ru265 can increase their lipophilicities [63]. To assess the influence of the methylphosphonate and diphenylphosphinate ligands of **1** and **2**, we measured their log *P* values. Although log *P* values are normally measured via the partition between a biphasic mixture of water and octanol, an analytical HPLC method that compares retention times to estimate log *P* values is also effective [69]. A calibration curve of measured HPLC retention factors (log *k*) and known log *P* values of reference compounds was created, enabling us to correlate the HPLC log *k* values of **1** and **2** to log *P* values. As shown in Figure 4, compound **2** is substantially more lipophilic (log *P* = 2.1) than Ru265, which has no retention on the HPLC column. The higher lipophilicity of **2** most likely arises from the hydrophobic phenyl groups of its axial ligands. By contrast, **1** also elutes within the column dead time, indicating that the compound is hydrophilic (log P $\leq$ –1.08). The log *P* value of the free diphenylphosphinic acid could not be measured via this method because of its long retention time (Figure S14, Supplemental Data). However, this analysis still allows us to conclude that the free ligand is more lipophilic than **2**. The positive charge and hydrophilic NH_3 ligands of the Ru265 core contribute to the lower log *P* value of **2** compared to the free diphenylphosphinic acid.

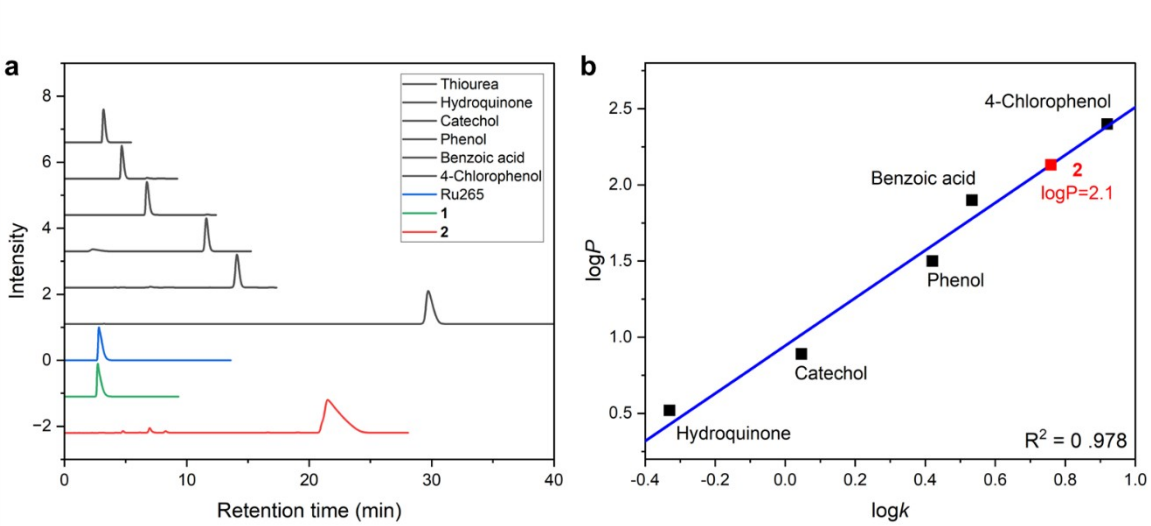

Figure 4. Measurement of log P values of Ru265, **1** and **2**. (a) HPLC chromatograms of reference compounds, Ru265, **1** and **2** eluted from C18 column at an isocratic gradient of 25% acetonitrile in H_2O with 0.1% trifluoroacetic acid. (b) The calibration curve between log P and log k ($k = (t–t_0)/t_0$) of reference compounds (black points). log P of **2** (red point) is calculated from the calibration curve.

3.3. Biological properties

Having characterized the new Ru265 derivatives, their biological properties were investigated. Because we are targeting MCU inhibitors for use as chemical biology tools and as cytoprotective agents, the possibility of undesirable cytotoxic effects needs to be measured. To probe their cytotoxicity, the compounds were administered to HeLa cells, and the cell viability after a 72-h incubation period was determined with the MTT assay. The IC_{50} values of **1** and **2** are >100 and ~90 μM (Table 2, Figure S15, Supplemental Data), respectively. These values are high, indicating that the compounds are not cytotoxic at the normal MCU-inhibition operating conditions employing a 2 h incubation with 50 μM concentrations. Next, the cell uptake properties of **1** and **2** were determined. HeLa cells were incubated with 50 μM of these test compounds for 2 h, harvested, and then lysed to measure Ru concentration by GFAAS and protein content by the BCA assay. As shown in Table 2, **1** is taken up to a similar extent to Ru265, whereas **2** accumulates in HeLa cells at 10-fold higher levels. Increased lipophilicity generally results in higher cell uptake [93,94], and this explanation may apply for our data for **2**, which is substantially more lipophilic than Ru265 and **1**. Although Ru265 cell uptake is believed to be mediated by organic cation transporter 3 (OCT3) [44], increasing the lipophilicity of its derivatives, like a ferrocene-capped analogue, has led to improved cellular uptake [63].

Table 2. Biological properties of Ru265**, 1** and **2**.

[a]

	Ru265	**1**	**2**
Cytotoxicity IC_{50} (μM)[a]	>100[c]	>100	~90
Cellular uptake (pg Ru/μg protein)[b]	56.3 ± 7.5	25.6 ± 2.1	511 ± 26
$_{m}Ca^{2+}$ uptake inhibition IC_{50} (nM)[d]	4.52 ± 0.02	26.3 ± 2.4	16.4 ± 3.7

72 h incubation in HeLa cells. [b] 2 h incubation in HeLa cells. [c] Ref. [61]
[d] In permeabilized HEK293T cells. Test compounds were prepared in aqueous solution without any pre-incubation.

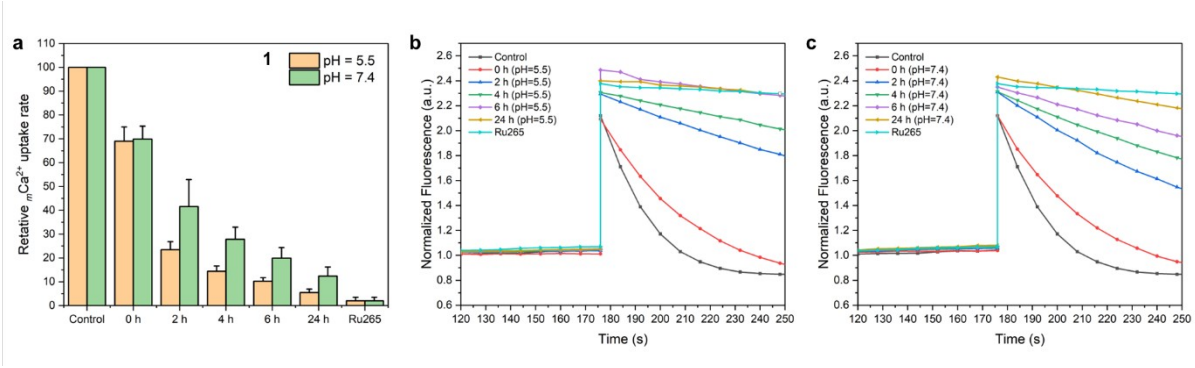

Figure 5. Comparison of MCU-inhibitory activity of **1** preincubated in different pH solutions. (a) Relative $_{m}Ca^{2+}$ uptake rate in permeabilized HEK293T cells treated with or without 20 nM of Ru265 or **1** pre-incubated at 37 °C under different pH for different period of time. Data are presented as mean ± SD, n = 3. (b and c) Representative traces of concentration changes of cytosolic Ca^{2+} (revealed by normalized fluorescence) in different treatment groups.

Having determined the cytotoxicity and cellular uptake properties of **1** and **2** in HeLa cells, their ability to inhibit the MCU in permeabilized HEK293T cells was assessed. The use of HEK293T cells for this assay was motivated by our prior extensive studies of other Ru265 analogues with these cells in this assay, as well as their higher growth rate, which facilitated the high cell count requirement for these experiments. The MCU-inhibitory activities of **1** and **2** without any preincubation period are summarized in Table 2 and Figure S16 (Supplemental Data). Although their IC_{50} values are in the nanomolar range, both **1** and **2** are less effective MCU inhibitors than Ru265. This result is consistent with other axially functionalized Ru265 analogues, which do not achieve their full inhibitory potential until after they undergo aquation. Accordingly, we assessed the MCU-inhibitory properties of **1** and **2** after preincubating them in aqueous solutions for different time periods. In addition, because the aquation of **1** is sensitive to pH, we sought to probe how solution pH affects the preincubation activation of this compound. Accordingly, a 20 nM solution of **1** was pre-incubated in physiological (pH = 7.4) and acidic (pH = 5.5) conditions at 37 °C for different periods of time prior to being assessed for their MCU-inhibitory properties in permeabilized HEK293T cells. As shown in Figure 5, preincubation of **1** in either buffer leads to improved inhibitory activity as quantified by the decrease in $_{m}Ca^{2+}$ uptake rate, a property that must arise from greater potency of the aquated product. However, even after 24 h of incubation, **1** does not reach the same potency as 20 nM Ru265. This result might be due to the fact that the primary

aquation product of **1** is the monoaquated complex rather than Ru265′. When comparing preincubation of this compound at the two pH values, **1** incubated at acidic pH is a more effective inhibitor than when incubated at physiological pH for all time points (Figure 5a), and this difference is apparent from the transient Ca^{2+} fluorescence traces (Figures 5b and 5c). This result is consistent with the faster aquation rate and higher aquation extent of **1** at lower pH.

The time- and pH-dependent MCU-inhibitory properties of **2** were also studied. As shown in Figure S17 (Supplemental Data), preincubation of **2** after 6 h releases full inhibitory potential that reaches the same potency as 15 nM of Ru265. This observation is consistent with the fact that **2** undergoes complete aquation to form the active species Ru265′. In comparing the treatments under different pH, no significant difference in inhibitory activity is observed. This result is obtained because the aquation kinetics of **2** in physiological and acidic conditions are comparable to each other. Therefore, the substantial difference between pH 7.4 and 5.5 observed for **1** most likely arises from the protonation equilibria available to the second OH group of the phosphonate ligand. This feature makes **1** valuable for selective activation in acidic environments. This property is valuable because many cells under pathological conditions, like ischemic cells and cancer cells in solid tumors, reside in regions with acidic pH values [95,96]. Thus, **1** could possibly be used to selectively target these conditions.

The potent inhibitory activity of **1** after preincubation is somewhat surprising because this compound does not fully aquate to form Ru265′. Therefore, we investigated the potential of the monoaquated product of **1** as a potential MCU inhibitor via molecular docking studies. The structure of the monoaquated complex $[Ru_2(\mu\text{-}N)(NH_3)_8(OPO(OH)Me)(OH_2)]^{4+}$ was first optimized with DFT (Table S3). Molecular docking [85] of the DFT-optimized monoaquated complex shows that it engages with the human MCU [84] via hydrogen-bonding interactions between its equatorial NH_3 and axial H_2O groups and aspartate and glutamate residues at the pore opening. Importantly, the methyphosphonate ligand does not appear to interfere with the hydrogen bonding of the other ligands. The monoaquated **1** has a comparable ChemPLP score (higher score represents better ligand docking [85]) as Ru265', meaning the compound can dock into the MCU pore as well as Ru265'. This result suggests that monoaquated analogues of Ru265 could also be valuable MCU inhibitors.

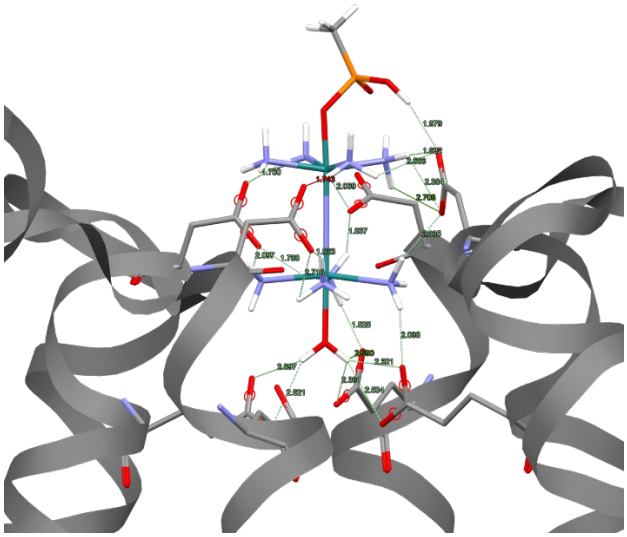

Figure 6. Molecular docking study showing interaction between monoaquated **1** and MCU (6O58) *[84]* at the opening pore (only chain A, C, E and G with ASP261 and GLU264 that participate in ligand interaction are shown for clarity). ChemPLP *[85]* score = 55.83 (Ru265' docking ChemPLP score = 51.15 *[60]*).

Given the promising results obtained in permeabilized cells, the MCU-inhibitory properties of **1** and **2** were also investigated in intact live HeLa cells. HeLa cells were used for this experiment for practical reasons, because they exhibited better adherence to the glass slides than HEK293T cells, allowing them to remain attached after multiple wash cycles at room temperature. HeLa cells were incubated with 50 μM of test compounds for 2 h, prior to being loaded with the mitochondria-localizing Rhod 2-AM Ca^{2+} sensor [97]. The HeLa cells were then treated with histamine to stimulate $_{m}Ca^{2+}$ uptake, which was monitored by the change of Rhod 2-AM fluorescence intensity via confocal microscopy. Untreated cells exhibited a 4.5-fold increase in fluorescence intensity, whereas cells pretreated with 50 μM of **1** and **2** for 2 h only underwent a 2.5–3-fold increase in intensity (Figure 7, Figure S18, Supplemental Data), reflecting their ability to inhibit $_{m}Ca^{2+}$ uptake. This result suggests that **1** and **2** can at least partially inhibit the MCU in these intact cells. To confirm that $_{m}Ca^{2+}$ uptake inhibition was not due to disruption of the mitochondrial membrane potential (MMP), we performed the JC-1 assay to assess the mitochondria viability in the presence of these compounds. This study verified that a 24-h incubation with 50 μM of **1** and **2** (Figure S19, Supplemental Data) in HeLa cells did not lead to disruption of the MMP, suggesting that diminished $_{m}Ca^{2+}$ uptake induced by these compounds arises from MCU inhibition. Because **2** is taken up by cells more effectively than Ru265 (Table 2), we investigated whether it could also inhibit the MCU in intact cells at lower concentrations. HeLa cells were pretreated with 10 or 50 μM of Ru265 or **2** for 2 h to assess their MCU-inhibitory activities at these concentrations. As shown in Figure 8 and Figure S20 (Supplemental Data), **2** is able to suppress $_{m}Ca^{2+}$ uptake at 10 μM, whereas Ru265 is unable to perform at this concentration.

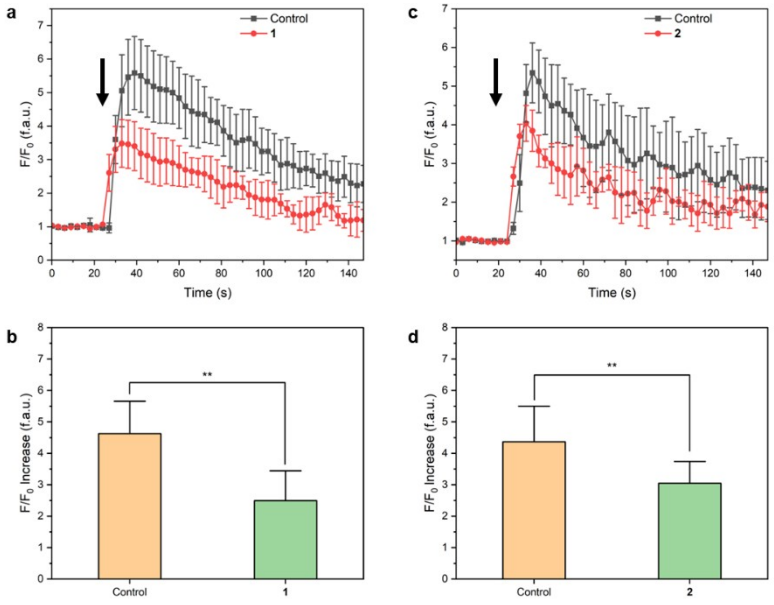

Figure 7. Change of $_{m}Ca^{2+}$ concentration in intact HeLa cells after addition of histamine (100 µM, indicated by an arrow), signified by the fluorescence change of Rhod 2-AM sensor over time, after incubating for 2 h in the presence of 50 µM (a) compound **1** or (c) compound **2**. The relative increase of Rhod2-AM fluorescence in response to histamine addition in the presence of either (b) **1** or (d) **2**, under the conditions described above. Data are presented as mean response ± SD, n =6.

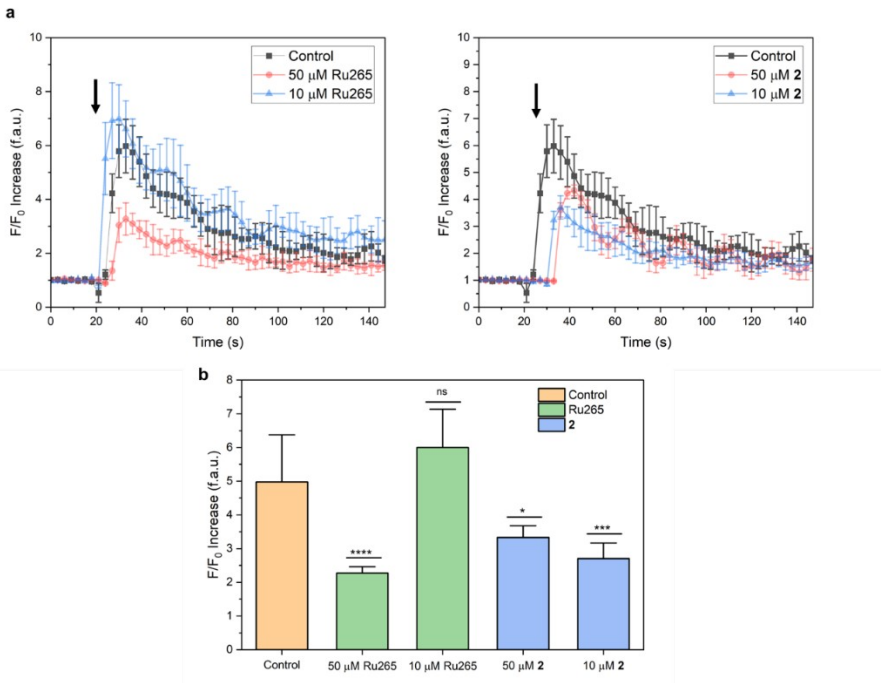

Figure 8. (a) Change of $_{m}Ca^{2+}$ concentration in intact HeLa cells after the addition of histamine (100 µM, marked by an arrow), signified by the fluorescence change of the Rhod2-AM sensor over time. Cells were pretreated for 2 h with or without Ru265 (left) or **2** (right) at 10 and 50 µM concentrations. (b) The relative

increase of Rhod 2-AM fluorescence in response to the addition of histamine (100 μM) in the presence of Ru265 and **2** at 10 and 50 μM concentrations. Data are presented as mean response ± SD, n =6.

4. Conclusion

Here, we have reported the preparation and properties of two new derivatives of Ru265 that contain axial phosphonate and phosphinate ligands. This work builds upon prior efforts to use carboxylate axial ligands for making Ru265 prodrugs. The use of these new axial ligands reveals interesting features that make them distinct from carboxylates. For example, **1**, which bears the methylphosphonate axial ligand, demonstrates some new features that have not yet been reported for this compound class. Unlike the carboxylates, this compound undergoes partial aquation, forming only the monoaquated complex in equilibrium with the starting material. The formation of this species suggests that the MCU-inhibitory properties can be more finely tuned and optimized via the modification of this axal ligand. Furthermore, the additional protonatable O atom on the methylphosphonate ligand provides a means of increasing the aquation rate of this compound under acidic conditions. This property is potentially valuable because many pathological conditions are characterized by having low-pH extracellular and intracellular environments. By contrast, the diphenylphosphinate ligands in **2** behave much more comparably to the carboxylates by exhibiting similar aquation half-lives and an enhancement of cellular uptake with increased lipophilicity. The new axial ligands presented in this study will provide access to additional Ru265 analogues by expanding the types of compounds that can serve as axial ligands for this compound class.

CRediT authorship contribution statement

Haipei Zou carried out chemical and biological experiments, analyzed the data and drafted the manuscript. Samantha N. MacMillan conducted X-ray diffraction data collection and solved the crystal structure. Justin J. Wilson conceptualized and designed the project, and reviewed and edited the manuscript.

Dedication

This article is dedicated to Professor Chris Orvig for his leadership in the field of metals in medicine, and for his continuous support young investigators in this area.

Declaration of competing interest

The authors declare no competing interests.

Acknowledgements

This work was supported by the University of California, Santa Barbara (UCSB) under the NSF award (CHE-2414429). This work made use of the Cornell University NMR facility and the UCSB NMR facility, which are supported by the NSF under award numbers CHE-1531632 and MRI-1920299, respectively. Imaging data from confocal microscopy was acquired through the Cornell

Institute of Biotechnology's Imaging Facility, with NIH 1S10RR025502 funding for the shared Zeiss LSM 710 Confocal Microscope.

Appendix A. Supplementary data

Supplementary data to this article including NMR and IR spectra, crystal data and structure refinement details, equations of first-order integrated rate law, microscopic imaging data, representative data analysis of biological assays, and optimized Cartesian coordinates obtained from DFT calculation can be found online. Crystallographic data for the structure of **1** have been deposited with the Cambridge Crystallographic Data Centre under deposition number 2493577. These can be accessed at http://www.ccdc.cam.ac.uk.

Data availability

Data will be made available from the authors upon reasonable request.

References

[1] D.E. Clapham, Calcium signaling, Cell 131 (2007) 1047–1058. https://doi.org/10.1016/j.cell.2007.11.028.

[2] E. Carafoli, J. Krebs, Why calcium? How calcium became the best communicator, J. Biol. Chem. 291 (2016) 20849–20857. https://doi.org/10.1074/jbc.R116.735894.

[3] C. Giorgi, S. Marchi, P. Pinton, The machineries, regulation and cellular functions of mitochondrial calcium, Nat. Rev. Mol. Cell Biol. 19 (2018) 713–730. https://doi.org/10.1038/s41580-018-0052-8.

[4] M.R. Duchen, Mitochondria and calcium: from cell signalling to cell death, J. Physiol. 529 (2000) 57–68. https://doi.org/10.1111/j.1469-7793.2000.00057.x.

[5] T.-I. Peng, M.-J. Jou, Oxidative stress caused by mitochondrial calcium overload, Ann. N. Y. Acad. Sci. 1201 (2010) 183–188. https://doi.org/10.1111/j.1749-6632.2010.05634.x.

[6] J.J. Lemasters, T.P. Theruvath, Z. Zhong, A.-L. Nieminen, Mitochondrial calcium and the permeability transition in cell death, Biochim. Biophys. Acta BBA - Bioenerg. 1787 (2009) 1395–1401. https://doi.org/10.1016/j.bbabio.2009.06.009.

[7] P.R. Angelova, A.Y. Abramov, Role of mitochondrial ROS in the brain: from physiology to neurodegeneration, FEBS Lett. 592 (2018) 692–702. https://doi.org/10.1002/1873-3468.12964.

[8] M. Calvo-Rodriguez, S.S. Hou, A.C. Snyder, E.K. Kharitonova, A.N. Russ, S. Das, Z. Fan, A. Muzikansky, M. Garcia-Alloza, A. Serrano-Pozo, E. Hudry, B.J. Bacskai, Increased mitochondrial calcium levels associated with neuronal death in a mouse model of Alzheimer's disease, Nat. Commun. 11 (2020) 2146. https://doi.org/10.1038/s41467-020-16074-2.

[9] E. Pchitskaya, E. Popugaeva, I. Bezprozvanny, Calcium signaling and molecular mechanisms underlying neurodegenerative diseases, Cell Calcium 70 (2018) 87–94. https://doi.org/10.1016/j.ceca.2017.06.008.

[10] D.J. Hausenloy, D.M. Yellon, Myocardial ischemia-reperfusion injury: a neglected therapeutic target, J. Clin. Invest. 123 (2013) 92–100. https://doi.org/10.1172/JCI62874.

[11] T. Kalogeris, C.P. Baines, M. Krenz, R.J. Korthuis, Cell biology of ischemia/reperfusion injury, Int. Rev. Cell Mol. Biol. 298 (2012) 229–317. https://doi.org/10.1016/B978-0-12-394309-5.00006-7.

[12] A.T. Turer, J.A. Hill, Pathogenesis of myocardial ischemia-reperfusion injury and rationale for therapy, Am. J. Cardiol. 106 (2010) 360–368. https://doi.org/10.1016/j.amjcard.2010.03.032.

[13] K.N. Belosludtsev, N.V. Belosludtseva, M.V. Dubinin, Diabetes mellitus, mitochondrial dysfunction and Ca^{2+}-dependent permeability transition pore, Int. J. Mol. Sci. 21 (2020) 6559. https://doi.org/10.3390/ijms21186559.

[14] C.-H. Wang, Y.-H. Wei, Role of mitochondrial dysfunction and dysregulation of Ca^{2+} homeostasis in the pathophysiology of insulin resistance and type 2 diabetes, J. Biomed. Sci. 24 (2017) 70. https://doi.org/10.1186/s12929-017-0375-3.

[15] Y. Liu, M. Jin, Y. Wang, J. Zhu, R. Tan, J. Zhao, X. Ji, C. Jin, Y. Jia, T. Ren, J. Xing, MCU-induced mitochondrial calcium uptake promotes mitochondrial biogenesis and colorectal cancer growth, Signal Transduct. Target. Ther. 5 (2020) 59. https://doi.org/10.1038/s41392-020-0155-5.

[16] C. Delierneux, S. Kouba, S. Shanmughapriya, M. Potier-Cartereau, M. Trebak, N. Hempel, Mitochondrial calcium regulation of redox signaling in cancer, Cells 9 (2020) 432. https://doi.org/10.3390/cells9020432.

[17] D. De Stefani, A. Raffaello, E. Teardo, I. Szabò, R. Rizzuto, A forty-kilodalton protein of the inner membrane is the mitochondrial calcium uniporter, Nature 476 (2011) 336–340. https://doi.org/10.1038/nature10230.

[18] J.M. Baughman, F. Perocchi, H.S. Girgis, M. Plovanich, C.A. Belcher-Timme, Y. Sancak, X.R. Bao, L. Strittmatter, O. Goldberger, R.L. Bogorad, V. Koteliansky, V.K. Mootha, Integrative genomics identifies MCU as an essential component of the mitochondrial calcium uniporter, Nature 476 (2011) 341–345. https://doi.org/10.1038/nature10234.

[19] J.J. Woods, J.J. Wilson, Inhibitors of the mitochondrial calcium uniporter for the treatment of disease, Curr. Opin. Chem. Biol. 55 (2020) 9–18. https://doi.org/10.1016/j.cbpa.2019.11.006.

[20] K. Márta, P. Hasan, M. Rodríguez-Prados, M. Paillard, G. Hajnóczky, Pharmacological inhibition of the mitochondrial Ca^{2+} uniporter: relevance for pathophysiology and human therapy, J. Mol. Cell. Cardiol. 151 (2021) 135–144. https://doi.org/10.1016/j.yjmcc.2020.09.014.

[21] A. Venugopal, M. Iyer, V. Balasubramanian, B. Vellingiri, Mitochondrial calcium uniporter as a potential therapeutic strategy for Alzheimer's disease, Acta Neuropsychiatr. 32 (2020) 65–71. https://doi.org/10.1017/neu.2019.39.

[22] D.M. Arduino, J. Wettmarshausen, H. Vais, P. Navas-Navarro, Y. Cheng, A. Leimpek, Z. Ma, A. Delrio-Lorenzo, A. Giordano, C. Garcia-Perez, G. Médard, B. Kuster, J. García-Sancho, D. Mokranjac, J.K. Foskett, M.T. Alonso, F. Perocchi, Systematic identification of MCU modulators by orthogonal interspecies chemical screening, Mol. Cell 67 (2017) 711-723.e7. https://doi.org/10.1016/j.molcel.2017.07.019.

[23] H. Zhao, S. Chen, N. Cao, W. Wu, G. Liu, J. Gao, J. Chen, T. Li, D. Lu, L. Zeng, H. Zhu, W. Zhang, Q. Xia, T. Li, T. Zhou, X.-M. Zhang, A.-L. Li, X. Pan, Berberine is a novel mitochondrial calcium uniporter inhibitor that disrupts MCU-EMRE assembly, Adv. Sci. 12 (2025) 2412311. https://doi.org/10.1002/advs.202412311.

[24] G.D. Marco, F. Vallese, B. Jourde, C. Bergsdorf, M. Sturlese, A.D. Mario, V. Techer-Etienne, D. Haasen, B. Oberhauser, S. Schleeger, G. Minetti, S. Moro, R. Rizzuto, D.D. Stefani, M. Fornaro, C. Mammucari, A high-throughput screening identifies MICU1 targeting compounds, Cell Rep. 30 (2020) 2321-2331.e6. https://doi.org/10.1016/j.celrep.2020.01.081.

[25] N. Kon, M. Murakoshi, A. Isobe, K. Kagechika, N. Miyoshi, T. Nagayama, DS16570511 is a small-molecule inhibitor of the mitochondrial calcium uniporter, Cell Death Discov. 3 (2017) 17045. https://doi.org/10.1038/cddiscovery.2017.45.

[26] V.T. Thu, H.-K. Kim, L.T. Long, S.-R. Lee, T.M. Hanh, T.H. Ko, H.-J. Heo, N. Kim, S.H. Kim, K.S. Ko, B.D. Rhee, J. Han, NecroX-5 prevents hypoxia/reoxygenation injury by inhibiting the mitochondrial calcium uniporter, Cardiovasc. Res. 94 (2012) 342–350. https://doi.org/10.1093/cvr/cvs122.

[27] J. Schwartz, E. Holmuhamedov, X. Zhang, G.L. Lovelace, C.D. Smith, J.J. Lemasters, Minocycline and doxycycline, but not other tetracycline-derived compounds, protect liver cells from chemical hypoxia and ischemia/reperfusion injury by inhibition of the mitochondrial calcium uniporter, Toxicol. Appl. Pharmacol. 273 (2013) 172–179. https://doi.org/10.1016/j.taap.2013.08.027.

[28] J. Santo-Domingo, L. Vay, E. Hernández-SanMiguel, C.D. Lobatón, A. Moreno, M. Montero, J. Alvarez, The plasma membrane Na^+/Ca^{2+} exchange inhibitor KB-R7943 is also a potent inhibitor of the mitochondrial Ca^{2+} uniporter, Br. J. Pharmacol. 151 (2007) 647–654. https://doi.org/10.1038/sj.bjp.0707260.

[29] A. De Mario, A. Tosatto, J.M. Hill, J. Kriston-Vizi, R. Ketteler, D. Vecellio Reane, G. Cortopassi, G. Szabadkai, R. Rizzuto, C. Mammucari, Identification and functional validation of FDA-approved positive and negative modulators of the mitochondrial calcium uniporter, Cell Rep. 35 (2021) 109275. https://doi.org/10.1016/j.celrep.2021.109275.

[30] P.J. Smith, S.A. Morgan, M.E. Fox, J.V. Watson, Mitoxantrone-DNA binding and the induction of topoisomerase II associated DNA damage in multi-drug resistant small cell lung cancer cells, Biochem. Pharmacol. 40 (1990) 2069–2078. https://doi.org/10.1016/0006-2952(90)90237-F.

[31] Y.N. Antonenko, T.I. Rokitskaya, A.J.L. Cooper, B.F. Krasnikov, Minocycline chelates Ca^{2+}, binds to membranes, and depolarizes mitochondria by formation of Ca^{2+}-dependent ion channels, J. Bioenerg. Biomembr. 42 (2010) 151–163. https://doi.org/10.1007/s10863-010-9271-1.

[32] E. Ahler, W.J. Sullivan, A. Cass, D. Braas, A.G. York, S.J. Bensinger, T.G. Graeber, H.R. Christofk, Doxycycline alters metabolism and proliferation of human cell lines, PLOS ONE 8 (2013) e64561. https://doi.org/10.1371/journal.pone.0064561.

[33] R. Payne, C. Li, E. Fernandez-Garcia, H. Vais, K. Foskett, The MCU inhibitor DS16570511 has off-target effects on mitochondrial membrane potential, Biophys. J. 116 (2019) 270a. https://doi.org/10.1016/j.bpj.2018.11.1461.

[34] M. Tillhon, L.M. Guamán Ortiz, P. Lombardi, A.I. Scovassi, Berberine: New perspectives for old remedies, Biochem. Pharmacol. 84 (2012) 1260–1267. https://doi.org/10.1016/j.bcp.2012.07.018.

[35] C.L. Moore, Specific inhibition of mitochondrial Ca^{++} transport by ruthenium red, Biochem. Biophys. Res. Commun. 42 (1971) 298–305. https://doi.org/10.1016/0006-291X(71)90102-1.

[36] K.C. Reed, F.L. Bygrave, The inhibition of mitochondrial calcium transport by lanthanides and Ruthenium Red, Biochem. J. 140 (1974) 143–155. https://doi.org/10.1042/bj1400143.

[37] J.H. Luft, Ruthenium red and violet. I. Chemistry, purification, methods of use for electron microscopy and mechanism of action, Anat. Rec. 171 (1971) 347–368. https://doi.org/10.1002/ar.1091710302.

[38] K.M. Broekemeier, R.J. Krebsbach, D.R. Pfeiffer, Inhibition of the mitochondrial Ca^{2+} uniporter by pure and impure ruthenium red, Mol. Cell. Biochem. 139 (1994) 33–40. https://doi.org/10.1007/BF00944201.

[39] W.L. Ying, J. Emerson, M.J. Clarke, D.R. Sanadi, Inhibition of mitochondrial calcium ion transport by an oxo-bridged dinuclear ruthenium ammine complex, Biochemistry 30 (1991) 4949–4952. https://doi.org/10.1021/bi00234a016.

[40] J. Emerson, M.J. Clarke, W.L. Ying, D.R. Sanadi, The component of "ruthenium red" responsible for inhibition of mitochondrial calcium ion transport. Spectra, electrochemistry, and aquation kinetics. Crystal structure of μ-O-$[(HCO_2)(NH_3)_4Ru]_2Cl_3$, J. Am. Chem. Soc. 115 (1993) 11799–11805. https://doi.org/10.1021/ja00078a019.

[41] M.A. Matlib, Z. Zhou, S. Knight, S. Ahmed, K.M. Choi, J. Krause-Bauer, R. Phillips, R. Altschuld, Y. Katsube, N. Sperelakis, D.M. Bers, Oxygen-bridged dinuclear ruthenium amine complex specifically inhibits Ca^{2+} uptake into mitochondria *in vitro* and *in situ* in single cardiac myocytes, J. Biol. Chem. 273 (1998) 10223–10231. https://doi.org/10.1074/jbc.273.17.10223.

[42] S.R. Nathan, N.W. Pino, D.M. Arduino, F. Perocchi, S.N. MacMillan, J.J. Wilson, Synthetic methods for the preparation of a functional analogue of Ru360, a potent inhibitor of mitochondrial calcium uptake, Inorg. Chem. 56 (2017) 3123–3126. https://doi.org/10.1021/acs.inorgchem.6b03108.

[43] J.J. Woods, J. Lovett, B. Lai, H.H. Harris, J.J. Wilson, Redox stability controls the cellular uptake and activity of ruthenium-based inhibitors of the mitochondrial calcium uniporter (MCU), Angew. Chem. Int. Ed. 59 (2020) 6482–6491. https://doi.org/10.1002/anie.202000247.

[44] J.J. Woods, N. Nemani, S. Shanmughapriya, A. Kumar, M. Zhang, S.R. Nathan, M. Thomas, E. Carvalho, K. Ramachandran, S. Srikantan, P.B. Stathopulos, J.J. Wilson, M. Madesh, A selective and cell-permeable mitochondrial calcium uniporter (MCU) inhibitor preserves mitochondrial bioenergetics after hypoxia/reoxygenation injury, ACS Cent. Sci. 5 (2019) 153–166. https://doi.org/10.1021/acscentsci.8b00773.

[45] P. Xu, S. Swain, R.J. Novorolsky, E. Garcia, Z. Huang, T.P. Snutch, J.J. Wilson, G.S. Robertson, R.B. Renden, The mitochondrial calcium uniporter inhibitor Ru265 increases neuronal excitability and reduces neurotransmission via off-target effects, Br. J. Pharmacol. 181 (2024) 3503–3526. https://doi.org/10.1111/bph.16425.

[46] K. Ait-Aissa, O.M. Koval, N.R. Lindsey, I.M. Grumbach, Mitochondrial Ca^{2+} uptake drives endothelial injury by radiation therapy, Arterioscler. Thromb. Vasc. Biol. 42 (2022) 1121–1136. https://doi.org/10.1161/ATVBAHA.122.317869.

[47] V. Costiniti, G.H.S. Bomfim, M. Neginskaya, G.-Y. Son, E. Mitaishvili, M. Giacomello, E. Pavlov, R.S. Lacruz, Mitochondria modulate ameloblast Ca^{2+} signaling, FASEB J. 36 (2022) e22169. https://doi.org/10.1096/fj.202100602R.

[48] Y. Eom, S.R. Kim, Y.-K. Kim, S.H. Lee, Mitochondrial calcium waves by electrical stimulation in cultured hippocampal neurons, Mol. Neurobiol. 61 (2024) 3477–3489. https://doi.org/10.1007/s12035-023-03795-w.

[49] M. Kerkhofs, R. La Rovere, K. Welkenhuysen, A. Janssens, P. Vandenberghe, M. Madesh, J.B. Parys, G. Bultynck, BIRD-2, a BH4-domain-targeting peptide of Bcl-2, provokes Bax/Bak-independent cell death in B-cell cancers through mitochondrial Ca^{2+}-dependent mPTP opening, Cell Calcium 94 (2021) 102333. https://doi.org/10.1016/j.ceca.2020.102333.

[50] A.M. Krstic, A.S. Power, M.-L. Ward, Visualization of dynamic mitochondrial calcium fluxes in isolated cardiomyocytes, Front. Physiol. 12 (2022). https://doi.org/10.3389/fphys.2021.808798.

[51] A. Marmolejo-Garza, I.E. Krabbendam, M.D.A. Luu, F. Brouwer, M. Trombetta-Lima, O. Unal, S.J. O'Connor, N. Majerníková, C.R.S. Elzinga, C. Mammucari, M. Schmidt, M. Madesh, E. Boddeke, A.M. Dolga, Negative modulation of mitochondrial calcium uniporter complex protects neurons against ferroptosis, Cell Death Dis. 14 (2023) 772. https://doi.org/10.1038/s41419-023-06290-1.

[52] R.J. Novorolsky, M. Nichols, J.S. Kim, E.V. Pavlov, J. J Woods, J.J. Wilson, G.S. Robertson, The cell-permeable mitochondrial calcium uniporter inhibitor Ru265 preserves cortical neuron respiration after lethal oxygen glucose deprivation and reduces hypoxic/ischemic brain injury, J. Cereb. Blood Flow Metab. 40 (2020) 1172–1181. https://doi.org/10.1177/0271678X20908523.

[53] R. Valencia, J.W. Kranrod, L. Fang, A.M. Soliman, B. Azer, X. Clemente-Casares, J.M. Seubert, Linoleic acid-derived diol 12,13-DiHOME enhances NLRP3 inflammasome activation in macrophages, FASEB J. 38 (2024) e23748. https://doi.org/10.1096/fj.202301640RR.

[54] Y.F. Yazicioglu, E. Marin, C. Sandhu, S. Galiani, I.G.A. Raza, M. Ali, B. Kronsteiner, E.B. Compeer, M. Attar, S.J. Dunachie, M.L. Dustin, A.J. Clarke, Dynamic mitochondrial transcription and translation in B cells control germinal center entry and lymphomagenesis, Nat. Immunol. 24 (2023) 991–1006. https://doi.org/10.1038/s41590-023-01484-3.

[55] Y.V. Medvedeva, E. Sharman, J.H. Weiss, Mechanisms of delayed ischemia/reperfusion evoked ROS generation in the hippocampal CA1 zone of adult mouse brain slices, Sci. Rep. 15 (2025) 23439. https://doi.org/10.1038/s41598-025-07070-x.

[56] J.L. Alves, R.M. Quinta-Ferreira, M.E. Quinta-Ferreira, C.M. Matias, Exploring different mechanisms of reactive oxygen species formation in hypoxic conditions at the hippocampal CA3 area, Mol. Cell. Endocrinol. 601 (2025) 112517. https://doi.org/10.1016/j.mce.2025.112517.

[57] H. Sasaki, I. Nakagawa, T. Furuta, S. Yokoyama, Y. Morisaki, Y. Saito, H. Nakase, Mitochondrial calcium uniporter (MCU) is involved in an ischemic postconditioning effect against ischemic reperfusion brain injury in mice, Cell. Mol. Neurobiol. 44 (2024) 32. https://doi.org/10.1007/s10571-024-01464-7.

[58] T.E. Huntington, R. Srinivasan, Astrocytic mitochondria in adult mouse brain slices show spontaneous calcium influx events with unique properties, Cell Calcium 96 (2021) 102383. https://doi.org/10.1016/j.ceca.2021.102383.

[59] A.G. Gómez-Valadés, M. Pozo, L. Varela, M.B. Boudjadja, S. Ramírez, I. Chivite, E. Eyre, R. Haddad-Tóvolli, A. Obri, M. Milà-Guasch, J. Altirriba, M. Schneeberger, M. Imbernón, A.R. Garcia-Rendueles, P. Gama-Perez, J. Rojo-Ruiz, B. Rácz, M.T. Alonso, R. Gomis, A. Zorzano, G. D'Agostino, C.V. Alvarez, R. Nogueiras, P.M. Garcia-Roves, T.L. Horvath, M. Claret, Mitochondrial cristae-remodeling protein OPA1 in POMC neurons couples Ca^{2+} homeostasis with adipose tissue lipolysis, Cell Metab. 33 (2021) 1820-1835.e9. https://doi.org/10.1016/j.cmet.2021.07.008.

[60] J.J. Woods, M.X. Rodriguez, C.-W. Tsai, M.-F. Tsai, J.J. Wilson, Cobalt amine complexes and Ru265 interact with the DIME region of the mitochondrial calcium uniporter, Chem. Commun. 57 (2021) 6161–6164. https://doi.org/10.1039/D1CC01623G.

[61] N.P. Bigham, Z. Huang, J. Spivey, J.J. Woods, S.N. MacMillan, J.J. Wilson, Carboxylate-capped analogues of Ru265 are MCU inhibitor prodrugs, Inorg. Chem. 61 (2022) 17299–17312. https://doi.org/10.1021/acs.inorgchem.2c02930.

[62] N.P. Bigham, R.J. Novorolsky, K.R. Davis, H. Zou, S.N. MacMillan, M.J. Stevenson, G.S. Robertson, J.J. Wilson, Supramolecular delivery of dinuclear ruthenium and osmium MCU inhibitors, Inorg. Chem. Front. 11 (2024) 5064–5079. https://doi.org/10.1039/D4QI01102C.

[63] Z. Huang, J.A. Spivey, S.N. MacMillan, J.J. Wilson, A ferrocene-containing analogue of the MCU inhibitor Ru265 with increased cell permeability, Inorg. Chem. Front. 10 (2023) 591–599. https://doi.org/10.1039/D2QI02183H.

[64] Z. Huang, S.N. MacMillan, J.J. Wilson, A fluorogenic inhibitor of the mitochondrial calcium uniporter, Angew. Chem. Int. Ed. 62 (2023) e202214920. https://doi.org/10.1002/anie.202214920.

[65] J.J. Woods, R.J. Novorolsky, N.P. Bigham, G.S. Robertson, J.J. Wilson, Dinuclear nitrido-bridged osmium complexes inhibit the mitochondrial calcium uniporter and protect cortical neurons against lethal oxygen–glucose deprivation, RSC Chem. Biol. 4 (2023) 84–93. https://doi.org/10.1039/D2CB00189F.

[66] G.M. Sheldrick, SHELXT – Integrated space-group and crystal-structure determination, Acta Crystallogr. Sect. Found. Adv. 71 (2015) 3–8. https://doi.org/10.1107/S2053273314026370.

[67] G.M. Sheldrick, A short history of SHELX, Acta Crystallogr. A 64 (2008) 112–122. https://doi.org/10.1107/S0108767307043930.

[68] P. Müller, Practical suggestions for better crystal structures, Crystallogr. Rev. 15 (2009) 57–83. https://doi.org/10.1080/08893110802547240.

[69] OECD, Test no. 117: partition coefficient (n-octanol/water), HPLC method, OECD, Paris, 2022. https://doi.org/10.1787/9789264069824-en.

[70] S.T. Smiley, M. Reers, C. Mottola-Hartshorn, M. Lin, A. Chen, T.W. Smith, G.D. Steele, L.B. Chen, Intracellular heterogeneity in mitochondrial membrane potentials revealed by a J-aggregate-forming lipophilic cation JC-1., Proc. Natl. Acad. Sci. 88 (1991) 3671–3675. https://doi.org/10.1073/pnas.88.9.3671.

[71] S. De Biasi, L. Gibellini, A. Cossarizza, Uncompensated polychromatic analysis of mitochondrial membrane potential using JC-1 and multilaser excitation, Curr. Protoc. Cytom. 72 (2015) 7.32.1-7.32.11. https://doi.org/10.1002/0471142956.cy0732s72.

[72] C.A. Schneider, W.S. Rasband, K.W. Eliceiri, NIH Image to ImageJ: 25 years of image analysis, Nat. Methods 9 (2012) 671–675. https://doi.org/10.1038/nmeth.2089.

[73] D. Pendin, R. Norante, A. De Nadai, G. Gherardi, N. Vajente, E. Basso, N. Kaludercic, C. Mammucari, C. Paradisi, T. Pozzan, A. Mattarei, A synthetic fluorescent mitochondria-targeted sensor for ratiometric imaging of calcium in live cells, Angew. Chem. Int. Ed. 58 (2019) 9917–9922. https://doi.org/10.1002/anie.201902272.

[74] J.T. Maxwell, C.-H. Tsai, T.A. Mohiuddin, J.Q. Kwong, Analyses of mitochondrial calcium influx in isolated mitochondria and cultured cells, J. Vis. Exp. (2018) 57225. https://doi.org/10.3791/57225.

[75] R.I. Fonteriz, S. de la Fuente, A. Moreno, C.D. Lobatón, M. Montero, J. Alvarez, Monitoring mitochondrial [Ca^{2+}] dynamics with rhod-2, ratiometric pericam and aequorin, Cell Calcium 48 (2010) 61–69. https://doi.org/10.1016/j.ceca.2010.07.001.

[76] M. Madesh, B.J. Hawkins, T. Milovanova, C.D. Bhanumathy, S.K. Joseph, S.P. RamachandraRao, K. Sharma, T. Kurosaki, A.B. Fisher, Selective role for superoxide in $InsP_3$ receptor–mediated mitochondrial dysfunction and endothelial apoptosis, J. Cell Biol. 170 (2005) 1079–1090. https://doi.org/10.1083/jcb.200505022.

[77] M. J. Frisch, G. W. Trucks, H. B. Schlegel, G. E. Scuseria, M. A. Robb, J. R. Cheeseman, G. Scalmani, V. Barone, G. A. Petersson, H. Nakatsuji, X. Li, M. Caricato, A. V. Marenich, J. Bloino, B. G. Janesko, R. Gomperts, B. Mennucci, H. P. Hratchian, J. V. Ortiz, A. F. Izmaylov, J. L. Sonnenberg, D. Williams-Young, F. Ding, F. Lipparini, F. Egidi, J. Goings, B. Peng, A. Petrone, T. Henderson, D. Ranasinghe, V. G. Zakrzewski, J. Gao, N. Rega, G. Zheng, W. Liang, M. Hada, M. Ehara, K. Toyota, R. Fukuda, J. Hasegawa, M. Ishida, T. Nakajima, Y. Honda, O. Kitao, H. Nakai, T. Vreven, K. Throssell, J. A. Montgomery, Jr., J. E. Peralta, F. Ogliaro, M. J. Bearpark, J. J. Heyd, E. N. Brothers, K. N. Kudin, V. N. Staroverov, T. A. Keith, R. Kobayashi, J. Normand, K. Raghavachari, A. P. Rendell, J. C. Burant, S. S. Iyengar, J. Tomasi, M. Cossi, J. M. Millam, M. Klene, C. Adamo, R. Cammi, J. W. Ochterski, R. L. Martin, K. Morokuma, O. Farkas,, J. B. Foresman, and D. J. Fox, Gaussian 16, Revision C.01, (2019).

[78] C. Lee, W. Yang, R.G. Parr, Development of the Colle-Salvetti correlation-energy formula into a functional of the electron density, Phys. Rev. B 37 (1988) 785–789. https://doi.org/10.1103/PhysRevB.37.785.

[79] A.D. Becke, Density-functional thermochemistry. III. The role of exact exchange, J. Chem. Phys. 98 (1993) 5648–5652. https://doi.org/10.1063/1.464913.

[80] W.J. Hehre, R. Ditchfield, J.A. Pople, Self—consistent molecular orbital methods. XII. Further extensions of Gaussian—type basis sets for use in molecular orbital studies of organic molecules, J. Chem. Phys. 56 (1972) 2257–2261. https://doi.org/10.1063/1.1677527.

[81] P.C. Hariharan, J.A. Pople, The influence of polarization functions on molecular orbital hydrogenation energies, Theor. Chim. Acta 28 (1973) 213–222. https://doi.org/10.1007/BF00533485.

[82] P.J. Hay, W.R. Wadt, *Ab initio* effective core potentials for molecular calculations. Potentials for K to Au including the outermost core orbitals, J. Chem. Phys. 82 (1985) 299–310. https://doi.org/10.1063/1.448975.

[83] G. Jones, P. Willett, R.C. Glen, A.R. Leach, R. Taylor, Development and validation of a genetic algorithm for flexible docking, J. Mol. Biol. 267 (1997) 727–748. https://doi.org/10.1006/jmbi.1996.0897.

[84] Y. Wang, N.X. Nguyen, J. She, W. Zeng, Y. Yang, X. Bai, Y. Jiang, Structural mechanism of EMRE-dependent gating of the human mitochondrial calcium uniporter, Cell 177 (2019) 1252-1261.e13. https://doi.org/10.1016/j.cell.2019.03.050.

[85] O. Korb, T. Stützle, T.E. Exner, Empirical scoring functions for advanced protein−ligand docking with PLANTS, J. Chem. Inf. Model. 49 (2009) 84–96. https://doi.org/10.1021/ci800298z.

[86] Y. Xie, D.W. Shaffer, A. Lewandowska-Andralojc, D.J. Szalda, J.J. Concepcion, Water oxidation by ruthenium complexes incorporating multifunctional bipyridyl diphosphonate ligands, Angew. Chem. Int. Ed. 55 (2016) 8067–8071. https://doi.org/10.1002/anie.201601943.

[87] J.M. Cross, N. Gallagher, J.H. Gill, M. Jain, A.W. McNeillis, K.L. Rockley, F.H. Tscherny, N.J. Wirszycz, D.S. Yufit, J.W. Walton, Pyridylphosphinate metal complexes: synthesis, structural characterisation and biological activity, Dalton Trans. 45 (2016) 12807–12813. https://doi.org/10.1039/C6DT01264G.

[88] G.R. Desiraju, Hydrogen bonds and other intermolecular interactions in organometallic crystals, J. Chem. Soc. Dalton Trans. (2000) 3745–3751. https://doi.org/10.1039/B003285I.

[89] M. McCann, E. Murphy, C. Cardin, M. Convery, Synthesis and properties of tetra-μ-acetatodiruthenium(II,III) phenylphosphinate and phenylphosphonate complexes: X-ray crystal structures of $[Ru_2(\mu\text{-}O_2CCH_3)_4(HPhPO_2)_2]H$ and $[Ru_2(\mu\text{-}O_2CCH_3)_4(PhPO_3H)_2]H{\cdot}H_2O$, Polyhedron 12 (1993) 1725–1731. https://doi.org/10.1016/S0277-5387(00)84604-5.

[90] T. Steiner, The Hydrogen Bond in the Solid State, Angew. Chem. Int. Ed. 41 (2002) 48–76. https://doi.org/10.1002/1521-3773(20020104)41:1<48::AID-ANIE48>3.0.CO;2-U.

[91] E.P. Serjeant, B. Dempsey, Ionisation constants of organic acids in aqueous solution, in: Int. Union Pure Appl. Chem. Comm. Electrochem. Data, Pergamon Press, Oxford, 1979.

[92] K. Moedritzer, pH dependence of phosphorus-31 chemical shifts and coupling constants of some oxyacids of phosphorus, Inorg. Chem. 6 (1967) 936–939. https://doi.org/10.1021/ic50051a017.

[93] X. Liu, B. Testa, A. Fahr, Lipophilicity and its relationship with passive drug permeation, Pharm. Res. 28 (2011) 962–977. https://doi.org/10.1007/s11095-010-0303-7.

[94] B. Testa, P. Crivori, M. Reist, P.-A. Carrupt, The influence of lipophilicity on the pharmacokinetic behavior of drugs: Concepts and examples, Perspect. Drug Discov. Des. 19 (2000) 179–211. https://doi.org/10.1023/A:1008741731244.

[95] Y. Kato, S. Ozawa, C. Miyamoto, Y. Maehata, A. Suzuki, T. Maeda, Y. Baba, Acidic extracellular microenvironment and cancer, Cancer Cell Int. 13 (2013) 89. https://doi.org/10.1186/1475-2867-13-89.

[96] E. Boedtkjer, S.F. Pedersen, The acidic tumor microenvironment as a driver of cancer, Annu. Rev. Physiol. 82 (2020) 103–126. https://doi.org/10.1146/annurev-physiol-021119-034627.

[97] A. Minta, J.P.Y. Kao, R.Y. Tsien, Fluorescent indicators for cytosolic calcium based on rhodamine and fluorescein chromophores, J. Biol. Chem. 264 (1989) 8171–8178. https://doi.org/10.1016/S0021-9258(18)83165-9.

[98] Y.V. Medvedeva, E. Sharman, J.H. Weiss, Mechanisms of delayed ischemia/reperfusion evoked ROS generation in the hippocampal CA1 zone of adult mouse brain slices, Sci. Rep. 15 (2025) 23439. https://doi.org/10.1038/s41598-025-07070-x.